


## PAPER

View Article Online  
View Journal | View Issue

Cite this: *Biomater. Sci.*, 2023, **11**, 5872

# Engineering a platelet-rich plasma-based multifunctional injectable hydrogel with photothermal, antibacterial, and antioxidant properties for skin regeneration†

Vajihe Alinezhad,<sup>a</sup> Kimia Esmaeilzadeh,<sup>b</sup> Hadi Bagheri,<sup>c</sup> Habib Zeighami,<sup>d</sup> Ali Kalantari-Hesari,<sup>e</sup> Rahim Jafari,<sup>b</sup> Pooyan Makvandi,<sup>f</sup> Yi Xu,<sup>g</sup> Hamidreza Mohammadi,<sup>h,i</sup> Mohammad-Ali Shahbazi,<sup>j,k</sup> and Aziz Maleki  <sup>\*a,c</sup>

Wound healing remains a significant challenge worldwide, necessitating the development of new wound dressings to aid in the healing process. This study presents a novel photothermally active hydrogel that contains platelet-rich plasma (PRP) for infected wound healing. The hydrogel was formed in a one pot synthesis approach by mixing alginate (Alg), gelatin (GT), polydopamine (PDA), and PRP, followed by the addition of CaCl<sub>2</sub> as a cross-linker to prepare a multifunctional hydrogel (AGC-PRP-PDA). The hydrogel exhibited improved strength and good swelling properties. PDA nanoparticles (NPs) within the hydrogel endowed them with high photothermal properties and excellent antibacterial and antioxidant activities. Moreover, the hydrogels sustained the release of growth factors due to their ability to protect PRP. The hydrogels also exhibited good hemocompatibility and cytocompatibility, as well as high hemostatic properties. In animal experiments, the injectable hydrogels effectively filled irregular wounds and promoted infected wound healing by accelerating re-epithelialization, facilitating collagen deposition, and enhancing angiogenesis. The study also indicated that near-infrared light improved the healing process. Overall, these hydrogels with antibacterial, antioxidant, and hemostatic properties, as well as sustained growth factor release, show significant potential for skin regeneration in full-thickness, bacteria-infected wounds.

Received 21st May 2023,  
Accepted 5th July 2023  
DOI: 10.1039/d3bm00881a  
rsc.li/biomaterials-science

<sup>a</sup>Department of Pharmaceutical Nanotechnology, School of Pharmacy, Zanjan University of Medical Sciences, 45139-56184 Zanjan, Iran.

E-mail: Maleki@zums.ac.ir

<sup>b</sup>Department of Medical Nanotechnology, School of Medicine, Zanjan University of Medical Sciences, Zanjan, Iran

<sup>c</sup>Zanjan Pharmaceutical Nanotechnology Research Center (ZPNRC), Zanjan 45139-56184, Iran

<sup>d</sup>Department of Microbiology, School of Medicine, Zanjan University of Medical Sciences, Zanjan 45139-56184, Iran

<sup>e</sup>Department of Pathobiology, Faculty of Veterinary Science, Bu-Ali Sina University, Hamadan 6516738695, Iran

<sup>f</sup>School of Engineering, Institute for Bioengineering, The University of Edinburgh, Edinburgh, EH9 3JL, UK

<sup>g</sup>Department of Science & Technology, Department of Urology, Nano Medical Innovation & Collaboration Group (NMICG), The Quzhou Affiliated Hospital of Wenzhou Medical University, Quzhou People's Hospital, Quzhou, China

<sup>h</sup>Pharmaceutical Sciences Research Center, Hemoglobinopathy Institute, Mazandaran University of Medical Sciences, Sari, Iran

<sup>i</sup>Department of Toxicology/Pharmacology, Faculty of Pharmacy, Mazandaran University of Medical Sciences, Sari, Iran

<sup>j</sup>Department of Biomedical Engineering, University Medical Center Groningen, University of Groningen, Antonius Deusinglaan 1, 9713 AV Groningen, The Netherlands

<sup>k</sup>W.J. Kolff Institute for Biomedical Engineering and Materials Science, University of Groningen, University Medical Center Groningen, Antonius Deusinglaan 1, 9713 AV Groningen, The Netherlands

† Electronic supplementary information (ESI) available. See DOI: <https://doi.org/10.1039/d3bm00881a>

## 1. Introduction

Wound healing is a significant global challenge, and the development of suitable wound dressings that promote all stages of the healing process, including hemostasis, inflammation, proliferation, and remodeling, is urgently needed.<sup>1–4</sup> Hydrogels are a promising type of wound dressing material for skin repair because they can absorb exudate and create a moist environment for wound regeneration.<sup>5,6</sup> Injectable hydrogels, in particular, can fill any irregular wound shape, providing a physical barrier that shields the wound area from bacterial infection quickly.<sup>7–9</sup> Numerous natural polymer-based hydrogels, such as chitosan, hyaluronic acid, and alginate, have been used as wound dressings to promote skin regeneration.<sup>10,11</sup> Alginate, a natural polysaccharide, can form biocompatible hydrogels through ionic cross-linking with multivalent cations (e.g., Ca<sup>2+</sup>, Sr<sup>2+</sup>, and Ba<sup>2+</sup>).<sup>12,13</sup> Gelatin, a commonly used natural macromolecule in biological sciences, is known for its excellent non-immunogenicity, biocompatibility, and biodegradability. Gelatin-based hydrogels have been extensively employed in designing and constructing injectable hydrogel dressings due to their similarity to the extracellular matrix (ECM), attractive fluid absorption properties, and pro-

motion of cell adhesion and proliferation.<sup>14</sup> Recently, metal cross-linked hydrogels using  $\text{Ca}^{2+}$ ,<sup>15</sup>  $\text{Fe}^{3+}$ ,<sup>16</sup>  $\text{Cu}^{2+}$ ,<sup>17</sup>  $\text{Zn}^{2+}$ ,<sup>18</sup> and  $\text{Ag}^+$ <sup>19</sup> have garnered increasing attention in the design and fabrication of multifunctional hydrogels. The metal ions not only acted as cross-linkers to produce hydrogels with high mechanical performances, but also the cations endowed the hydrogels with high healing properties. Bacterial infection can impede the healing process of an infected wound, resulting in serious tissue damage and even life-threatening complications. Photothermal therapy (PTT) is a promising strategy that combines near-infrared light (NIR) (700–1100 nm) and light-absorbing materials to kill bacteria by inducing local hyperthermia during the PTT process.<sup>20</sup> PDA NPs have emerged as an effective photothermal agent in PTT of infected wounds due to their facile synthesis, long-term safety, high biodegradability, superior biocompatibility, and excellent photostability.<sup>21,22</sup> The unique properties of PDA endow NIR-responsive hydrogels with high cell/tissue adhesive, intrinsic antioxidant, and antibacterial properties.<sup>23,24</sup> Hemostasis, inflammation, proliferation, and dermal remodeling are four consecutive and overlapping steps involved in the wound healing process.<sup>8</sup> Additionally, many growth factors, chemokines, and cytokines play an essential role in this complex process.<sup>25</sup> Recent studies have shown that platelet-rich plasma (PRP), containing a high concentration of platelet-oriented plasma, has the potential to improve wound healing. PRP contains numerous growth factors, including vascular endothelial growth factor (VEGF), platelet-derived growth factor, and transforming growth factor- $\beta$  (TGF- $\beta$ ), which significantly contribute to regenerative medicine and wound repair.<sup>26,27</sup> These factors interact with the local environment to accelerate cell proliferation and differentiation, thus promoting angiogenesis and re-epithelialization through extracellular matrix synthesis and mesenchymal cell recruitment.<sup>28</sup> However, the application of PRP in wound healing is limited due to its short half-life, burst release, and high cost of synthesis.<sup>29,30</sup> Therefore, addressing how to reduce burst release, retain activity, and design a cost-effective method is crucial when using PRP-based tissue engineering. In this study, an injectable, photo-thermally PRP-loaded hydrogel is developed for infected dermal wound healing. The hydrogels were constructed based on alginate and gelatin cross-linked by  $\text{Ca}^{2+}$  ions (abbreviated as AGC) and PDA as a photothermal agent. After blood collection and centrifugation at different rates to fractionate the blood, the PRP fraction was isolated as the yellowish layer of plasma (Fig. 1). To prepare the AGC-PRP-PDA hydrogel, alginate, gelatin, PDA NPs, and PRP were mixed to produce a homogeneous polymeric solution. Subsequently, a mixture of thromboplastin (TPL) and  $\text{CaCl}_2$  was added to the previous mixture to form the multifunctional hydrogel (Fig. 1).  $\text{CaCl}_2$  not only acts as a cross-linker to induce gelation, but also activates PRP from a dynamic liquid to a gel, containing a large number of growth factors. We also used TPL in the fabrication of the hydrogels, resulting in a more homogeneous mixture. TPL can accelerate blood coagulation through the conversion of prothrombin to thrombin.<sup>31,32</sup> In addition, we also prepared

a platelet poor plasma (PPP)-containing hydrogel (AGC-PPP-PDA) to compare its therapeutic effect with AGC-PRP-PDA.

## 2. Materials and methods

### 2.1 Materials

Gelatin (15% (w/v), Fig. S4B,† type B, from bovine skin), sodium alginate (2.5% (w/v), Fig. S4C†), dopamine hydrochloride, Dulbecco's Modified Eagle's Medium (DMEM), fetal bovine serum (FBS), penicillin/streptomycin and 3-[4,5-dimethylthiazole-2-yl]-2,5-diphenyltetrazolium bromide (MTT) were purchased from Sigma-Aldrich. NIH3T3 cells were obtained from the Iranian Biological Resource Center (ATCC, CRL-1658). Calcium chloride (Merck, Germany) and the other reagents were analytically pure and used as received.

### 2.2 Preparation of PRP and PPP

PRP and PPP were obtained from Sprague-Dawley rat's blood in consensus with the guidelines of Zanjan University of Medical Sciences, Zanjan, Iran (ethical code: IR.ZUMS.REC.1400.071). PRP and PPP were collected from the rat's peripheral blood using the double-spin method.<sup>33</sup> Briefly, the rat's peripheral blood was collected in tubes containing an anticoagulant. Then, the two consecutive stages of centrifugation were carried out following particular parameters (first, 1600 rpm for 12 min and second, 2500 rpm for 5 min at room temperature) to optimize the production of PRP and PPP. Finally, 2/3 of supernatant was collected as PPP, and the remaining plasma and platelets were mixed and considered as PRP.

### 2.3 Preparation of PRP and AGC hydrogels

PRP gel was prepared by the activation of PRP by  $\text{CaCl}_2$  (100  $\mu\text{L}$ , 2% w/v) and TPL (100  $\mu\text{L}$ , 22.08  $\text{mg mL}^{-1}$ ). To fabricate the AGC hydrogel, 200  $\mu\text{L}$  of sodium alginate (2.5% w/v) and 100  $\mu\text{L}$  of gelatin (15% w/v) were firstly mixed to make a homogeneous mixture. Then, 50  $\mu\text{L}$  of  $\text{Ca}^{2+}$  solution (2% w/v) was added into the previous mixture to obtain the AGC hydrogel.

### 2.4 Preparation of AGC-PRP-PDA and AGC-PPP-PDA hydrogels

For fabrication of the AGC-PRP-PDA hydrogel, 400  $\mu\text{L}$  of sodium alginate solution (2.5% w/v), 200  $\mu\text{L}$  of gelatin solution (15% w/v), 200  $\mu\text{L}$  of PRP solution, and 10  $\mu\text{L}$  of PDA NPs (5  $\text{mg mL}^{-1}$ ) were firstly mixed to make a homogeneous solution. Then, a pre-prepared mixture of 200  $\mu\text{L}$  of  $\text{Ca}^{2+}$  solution (2% w/v) and 100  $\mu\text{L}$  of TPL (22.08  $\text{mg mL}^{-1}$ ) was added to the above mixture to form the AGC-PRP-PDA hydrogel. The AGC-PPP-PDA hydrogel was prepared using the same procedure with the difference that PPP was used instead of PRP.

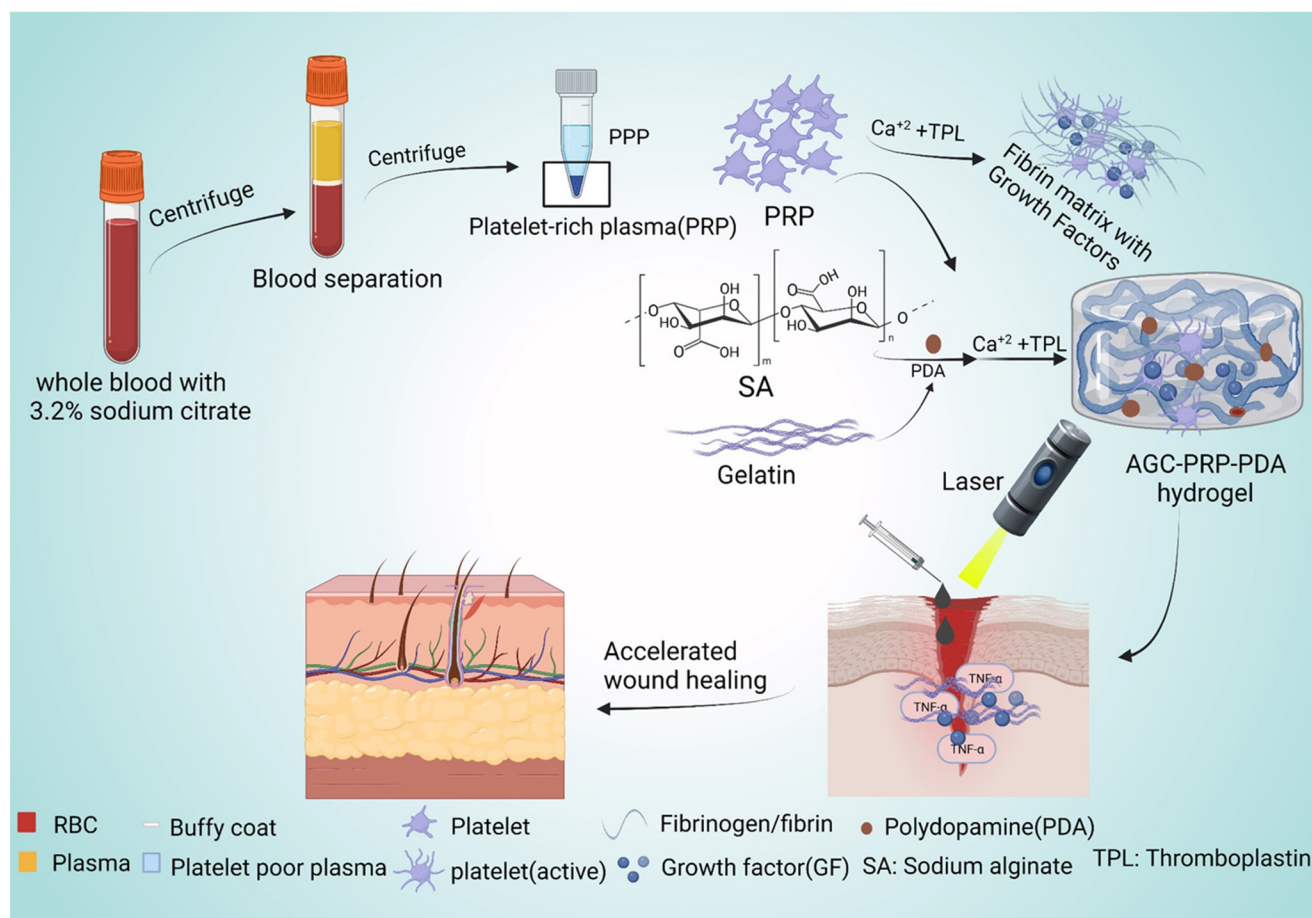


**Fig. 1** Schematic representation of the preparation of PRP and PPP as well as the synthetic route of the AGC-PRP-PDA hydrogel with multiple functionalities to promote wound regeneration.

## 2.5 Synthesis of PDA NPs

PDA NPs with an average diameter of 170–180 nm were synthesized according to a previous report.<sup>34</sup> Briefly, ammonia aqueous solution (1 mL, 28–30%) was added into a mixture of ethanol (20 mL) and deionized water (45 mL) under mild stirring at 30 °C for 30 min. Then, dopamine hydrochloride (0.25 g), dissolved in deionized water (5 mL), was added dropwise into the previous solution. The color of the resulting solution turned pale yellow and gradually changed to dark brown. After 24 h, the final product was obtained by centrifugation and was washed with deionized water three times and then dispersed in deionized water.

## 2.6 Characterization of the PDA NPs and the hydrogels

The microstructure and morphology of the hydrogels were determined by scanning electron microscopy (SEM) (Quanta 250 FEG, USA).

The formation of the hydrogels was confirmed by Fourier transform infrared spectroscopy (FTIR) (Bruker, Tensor 27, Germany). The UV-vis-NIR analysis of PDA NPs and the AGC-PRP-PDA hydrogel was performed using a UV-vis spectro-

photometer (Bruker IFS 66v/s). The zeta potential of PDA NPs was measured by dynamic light scattering (DLS) (Malvern, UK).

## 2.7 Swelling and *in vitro* degradation of the AGC-PRP-PDA hydrogel

A weighted cylindrical freeze-dried hydrogel ( $S_0$ ) was incubated in PBS solution (pH ~ 7.4) at room temperature. At pre-determined intervals, the hydrogel was carefully taken out, and the residual water on the surface was removed using filter paper and weighed ( $S_1$ ). The swelling percentage was measured using the following formula:

$$\text{Swelling percentage} = S_1/S_0 \times 100, \quad (1)$$

where  $S_0$  represents the initial weight of the hydrogel at time 0 h and  $S_1$  is the weight of the hydrogel at different times.<sup>35</sup>

An *in vitro* gel degradation assay was carried out based on a previous report.<sup>35,36</sup> Briefly, the cylindrical freeze-dried hydrogels were weighed ( $W_0$ ) and incubated in PBS solution (pH ~ 7.4). At predetermined intervals, the residual hydrogels were carefully taken out from the solution, and freeze-dried and

weighed ( $W_t$ ). The percentage of the remaining weight was measured using the following equation:

$$\text{Weight remaining (\%)} = W_t/W_0 \times 100, \quad (2)$$

where  $W_0$  and  $W_t$  are the weights of the AGC-PRP-PDA hydrogel before and after degradation, respectively.

## 2.8 Molecular docking

The structure of the alginate fragment was constructed using the block co-polymer builder of Materials Studio software. The model consisted of 2 and 3 consecutive units of  $\alpha$ -L-guluronic acid (G) and  $\beta$ -D-mannuronic acid (M), respectively (GGMMM). This alginate sequence contains all three types of G-G, M-M and G-M bonds. For the gelatin material, with the help of an in-house script, a portion of the collagen type I alpha 1 sequence (UniProt ID: Q6LAN8) was carefully chosen in such a way that it represents the common sequence motifs and amino acid composition of collagen proteins as closely as possible. The initial 3D structure of the collagen fragment with the sequence of Gly-Pro-Ala-Gly-Arg-Pro-Gly-Glu-Val was predicted using the SWISS Model server. The final structure of the peptide was built by manual conversion of the structure of the second proline (position 6) to the 4-hydroxy proline. The structures of both ligands (alginate and collagen) were then geometry optimized using Avogadro software. The molecular structures of the growth factors VEGF-A (PDB ID: 5T89) and TGF- $\beta$  (PDB ID: 1KLC) were obtained from the Protein Data Bank (PDB). Docking input files were prepared using AutoDock tools (ADT) version 1.5.6. The sizes of the grid boxes were adjusted to include the entire structure of the target molecules. The docking simulations were performed using AutoDock version 4.2.6. The Lamarckian genetic algorithm with default search parameters, with the exception of a larger number of runs ( $n = 500$ ), was used to predict possible hydrogel-growth factor interaction sites and binding energies. Visualization and binding site analysis of the top-ranked poses were performed using PyMol software.

## 2.9 Rheological measurements of the hydrogels

The viscoelastic properties of the hydrogels were determined by a frequency sweep test (MCR300, Anton Paar, USA), at the frequency of 0.01–100 Hz to obtain the storage modulus ( $G'$ ) and loss modulus ( $G''$ ). The viscosity of AGC, AGC-PPP-PDA, and AGC-PRP-PDA hydrogels against the shear rate was determined with parallel plate geometry (75 mm diameter) at room temperature using a rheometer (R/S Brookfield, Canada) to confirm shear thinning properties.

## 2.10 Photothermal evaluation of the hydrogel

The photothermal performance of the AGC-PRP-PDA hydrogel and PDA NPs with different concentrations was investigated using an 808 nm NIR laser at power densities of 0.5, 1, and 1.5 W cm<sup>-2</sup> for 10 min. The temperature was recorded using an infrared thermal camera (TiS55, Fluke, USA). The photother-

mal stability of the AGC-PRP-PDA hydrogel was measured by five cycles of laser on-off. To this end, 1 mL of the hydrogel was irradiated under 808 nm (1 W cm<sup>-2</sup>) for 10 min (laser on for 10 min per cycle). The temperature was recorded every minute using the infrared thermal camera. The photothermal conversion efficiency ( $\eta$ ) of the AGC-PRP-PDA hydrogel was calculated using the following equation:<sup>7,37,38</sup>

$$\eta = \frac{hs(T_{\max} - T_{\text{surr}}) - Q_0}{I(1 - 10^{-A_{808}})} \quad (3)$$

Hence, first, the time constant of heat transfer ( $\tau_s$ ) was calculated by linear time data *versus*  $-\ln(\theta)$  from the cooling phase, as follows:

$$\tau_s = \frac{t}{-\ln(\theta)}. \quad (4)$$

The  $\theta$  value was measured using the equation:

$$\theta = \frac{T - T_{\min}}{T_{\max} - T_{\min}} \quad (5)$$

where  $T$  refers to the temperature in each time point.

Then, ( $hs$ ) was measured using the following equation:

$$hs = \frac{m_i c_i}{\tau_s}. \quad (6)$$

After that, deionized water (solvent) (1 mL) was irradiated using an 808 nm laser for 10 min and the temperature was recorded in the cooling phase and all the above-mentioned processes were repeated for the solvent.  $Q_0$  is the heat associated with the light absorbance of the solvent. It was calculated using the following equation:

$$Q_0 = hs(T_{\max, \text{water}} - T_{\text{surr}}) \quad (7)$$

$T_{\max, \text{water}} - T_{\text{surr}}$  was measured between the maximum temperature of deionized water and the surrounding temperature. Finally, the  $\eta$  value was obtained, where  $h$  is the heat transfer coefficient,  $s$  is the surface area of the container,  $Q_0$  is the heat associated with the light absorbance of the solvent,  $m_i$  is the weight of the dried hydrogel, and  $c_i$  is the heat capacity of the solvent, which is 4.2 J g<sup>-1</sup> K<sup>-1</sup>.  $A_{808}$  is the absorbance of PDA NPs at the wavelength of 808 nm.

## 2.11 *In vitro* antibacterial activity of the hydrogels

*Staphylococcus aureus* (*S. aureus*, ATCC25923) and *Escherichia coli* (*E. coli*, ATCC25922) were used to evaluate the antibacterial activity of the hydrogels. Bacteria were cultured in a Brain Heart Infusion (BHI) broth/agar (Merck, Germany) aerobically at 37 °C for 18–24 h. The antibacterial effect of the hydrogels was evaluated by the spread plate method for colony counting of *E. coli* and *S. aureus*. A volume of the as-prepared bacterial suspension (20  $\mu$ L,  $1.5 \times 10^8$  CFU mL<sup>-1</sup>) was added into 1 mL of all the hydrogel groups and normal saline as the control group. The NIR-treated groups were exposed to 808 nm light for 10 min (1 W cm<sup>-2</sup>). After incubation for 2 h, the bacterial solution was further re-sus-



pended and diluted 30 times. Then, 100  $\mu\text{L}$  of the diluted bacterial solution was spread on nutrient agar (Merck, Germany) and incubated for 18–24 h. Bacterial colonies were counted in each sample and the bacterial survival ratio was calculated as follows:<sup>38,39</sup>

$$\text{Bacterial survival ratio}\% = \frac{(N \text{ in the sample}/N \text{ in the control}) \times 100,}{(8)}$$

where  $N$  is the colony number on a plate.

## 2.12 *In vitro* antibacterial activity of PDA NPs

The spread plate method was carried out to investigate the antibacterial effect of PDA NPs. 20  $\mu\text{L}$  of the as-prepared *E. coli* or *S. aureus* suspension ( $1.5 \times 10^8$  CFU  $\text{mL}^{-1}$ ) was added into 1 mL of LB broth containing 5  $\text{mg mL}^{-1}$  PDA NPs. 1 mL of LB broth containing the same amount of the bacterial suspension was considered as the control group. The NIR-treated groups were exposed to 808 nm laser irradiation for 10 min (1 W  $\text{cm}^{-2}$ ). After incubation for 2 h, the bacterial solution was diluted using normal saline, and subsequently, 100  $\mu\text{L}$  of the diluted solution was spread on the agar plate and incubated at 37 °C for 18–24 h. Finally, bacterial colonies were counted in each plate. At least two samples on each group were tested and the bacterial survival ratio% was expressed as:

$$\text{Bacterial survival ratio}\% = \frac{(N \text{ in the sample}/N \text{ in the control}) \times 100,}{(9)}$$

where  $N$  is the colony number on a plate.<sup>40,41</sup>

## 2.13 Antioxidant capacity of the hydrogels

The efficiency of the free radical scavenging performance of the AGC, AGC-PPP-PDA, and AGC-PRP-PDA hydrogels was studied using 1,1-diphenyl-2-picryl-hydrazyl (DPPH) as an indicator, which is commonly used to assess the reactive nitrogen species (RNS) scavenging capacity of the materials. First, 500  $\mu\text{M}$  DPPH and the desired amount of the AGC-PRP-PDA hydrogel (1, 2, 3, and 4 mg) were dispersed in 3 mL of ethanol. Then, the mixture was stirred in a dark place at room temperature for half an hour. Finally, the absorbance change of DPPH was measured using a UV-vis spectrophotometer. DPPH scavenging activity was studied using the following equation:<sup>42</sup>

$$\text{DPPH scavenging } (\%) = (A_b - A_s)/A_b \times 100, \quad (10)$$

where  $A_b$  is the absorption of the blank (DPPH + ethanol) and  $A_s$  is the absorption of the sample (DPPH + sample + ethanol). A  $\text{H}_2\text{O}_2$  scavenging assay was performed using a previously reported study.<sup>43,44</sup> 6  $\text{mg mL}^{-1}$  and 10  $\text{mg mL}^{-1}$  AGC-PRP-PDA gels were blended with 0.8 mL of freshly prepared 40 mM  $\text{H}_2\text{O}_2$  solution. Similar concentrations of ascorbic acid were used as a positive control. The reaction blends were incubated at room temperature for 30 min, and the absorbance of the samples was measured at 230 nm using a UV-visible spectrophotometer.

## 2.14 Hemolysis assay

An *in vitro* hemolysis test was performed using an erythrocyte suspension according to previously reported protocols.<sup>45</sup> Whole anticoagulant blood was centrifuged with PBS (pH 7.4) at 3000 rpm for 6 min to obtain fresh red blood cells (RBCs). The purified RBCs were washed five times and diluted to a concentration of 5% (v/v). Afterward, 500  $\mu\text{L}$  of PBS solution (pH 7.4) containing different amounts of hydrogels were mixed with RBC suspensions (100  $\mu\text{L}$ ) to obtain the mixtures with different concentrations (0.25, 0.5, and 1  $\text{mg mL}^{-1}$ ). PBS solution and deionized water were used as the negative and positive control groups, respectively. After incubation at 37 °C for 2, 4, 8, and 24 h, all mixtures were centrifuged at 3000 rpm for 6 min. The supernatant (150  $\mu\text{L}$ ) was transferred to a 96-well plate, and the absorbance at 540 nm was measured using a microplate reader. The hemolysis ratio was measured using the following equation:

$$\text{Hemolysis ratio } (\%) = [(A_s - A_n)/(A_p - A_n)] \times 100, \quad (11)$$

or

$$\text{Non-hemolysis ratio } (\%) = 1 - [(A_s - A_n)/(A_p - A_n)] \times 100, \quad (12)$$

where  $A_s$ ,  $A_n$ , and  $A_p$  are the absorbance of a hydrogel, PBS, and deionized water, respectively.

## 2.15 *In vitro* cytotoxicity of the hydrogels

The cytotoxicity of the hydrogels was determined by an MTT assay. In order to perform the cell viability assay, mouse embryo fibroblast cells (NIH3T3) were cultured in DMEM with 10% fetal bovine serum and 1% penicillin-streptomycin solution in a  $\text{CO}_2$  incubator at 37 °C. NIH3T3 cells were seeded at a density of  $2 \times 10^6$  cells per mL in 96 well plates. After 24 h, the culture medium was replaced by 200  $\mu\text{L}$  of aqueous suspensions of AGC, AGC-PPP-PDA, and AGC-PRP-PDA (1  $\text{mg mL}^{-1}$ , 500  $\mu\text{g mL}^{-1}$ , and 250  $\mu\text{g mL}^{-1}$ ). After incubation for 48 and 72 h, the medium was replaced with 180  $\mu\text{L}$  of fresh medium and 20  $\mu\text{L}$  of MTT (5 mg in PBS (1 mL)), followed by incubation for another 4 h to allow formation of the formazan dye. The medium was then replaced by 200  $\mu\text{L}$  of dimethylsulfoxide per well to dissolve the purple formazan, and the absorbance was measured using a microplate reader at 570 nm. The cell viability ratio was calculated using the following formula:

$$\text{Cell viability} = A_s/A_c \times 100, \quad (13)$$

where  $A_s$  and  $A_c$  represent the absorbance of the sample and the control group, respectively.

## 2.16 *In vitro* blood clotting index

50 mg of freeze-dried AGC, AGC-PPP-PDA, and AGC-PRP-PDA hydrogels and gauze were placed into pre-heated falcon tubes at 37 °C. Sodium citrate whole blood (100  $\mu\text{L}$ ) was added on to the hydrogel surface, followed by addition of 12.5  $\mu\text{L}$  of 0.2 M  $\text{CaCl}_2$  solution to start coagulation. The tubes were incubated in 37 °C. After 60, 120, and 240 s, 10 mL of deionized water

was added to each tube. Subsequently, the samples were centrifuged at 1000 rpm for 5 min. Finally, the absorbance of the resulting hemoglobin solution was measured at 540 nm. The blood clotting index (BCI) was calculated using the following equation:

$$\text{BCI (\%)} = A_s/A_r \times 100, \quad (14)$$

where  $A_s$  and  $A_r$  are the absorption of the sample or gauze and deionized water as references, respectively.

### 2.17 *In vivo* hemostatic performance

A mouse-tail amputation model was employed to evaluate the hemostatic ability of the hydrogels. All animal studies were approved by the animal research Zanjan University of Medical Sciences' Animal Ethics Committee (IR.ZUMS.REC.1400.071). The rats (Sprague-Dawley rats, male, 200–250 g) were anesthetized using ketamine/xylazine (6 : 4, v/v). Then, the middle of the tail was cut with surgical bistoury. After cutting, the tail of the mouse was placed in air for 15 s to ensure normal blood loss. After that, the tail was covered with a pre-weighted freeze-dried hydrogel powder under slight pressure. The data of hemostatic time and blood loss were measured as the hemostatic performance. The group without the treatment was used as the control.<sup>46</sup>

### 2.18 Growth factor release study

To evaluate the release profile of VEGF and TGF- $\beta$  of the hydrogels, 400  $\mu\text{L}$  of the PRP gel (containing 200  $\mu\text{L}$  of PRP) and  $\sim 1100$   $\mu\text{L}$  of the AGC-PRP-PDA hydrogel (containing 200  $\mu\text{L}$  of PRP) were placed in a 24 well plate ( $n = 3$ ) with 1.5 mL of PBS (pH 7.4) as the release medium. The well plate was incubated at 37 °C (1 rpm). 150  $\mu\text{L}$  of PBS was collected at a pre-determined time interval, while 150  $\mu\text{L}$  of fresh PBS was replaced. The collected PBS was stored at  $-20$  °C for further tests. Finally, the concentrations of VEGF and TGF- $\beta$  were measured using an ELISA kit following the manufacturer's protocol.<sup>47–49</sup>

### 2.19 *In vitro* wound healing (scratch assay)

The *in vitro* wound healing potential of the hydrogels was assessed using NIH3T3 fibroblast cells. To this end, NIH3T3 cells were seeded at a density of  $5 \times 10^5$  cells per mL on 24 well plates to obtain a monolayer of the cells. The cells were starved using DMEM medium and 0.1% FBS with 5% penicillin/streptomycin for 24 h at 37 °C, preventing the cells from proliferating to ensure that wound closure results solely from cell migration.<sup>50</sup> Next, an artificial wound was generated to create a scratch with a p100 pipette tip and then the debris was removed using a culture medium. 500  $\mu\text{L}$  of the suspension of the AGC-PPP-PDA and AGC-PRP-PDA hydrogels (250  $\mu\text{g mL}^{-1}$ ) dispersed in the fresh culture medium DMEM supplemented with 10% FBS were added into each well plate. The group without any treatment was considered as the control group. The cell migration of each group at 0 h, 10 h, and 24 h was re-photographed using a phase contrast microscope. The

quantitative analysis was performed using the following formula:<sup>51</sup>

$$\text{Relative scratch area (\%)} = A_n/A_0 \times 100, \quad (15)$$

where  $A_0$  represents the initial area at 0 h and  $A_n$  is the area at different times.

### 2.20 *In vivo* wound healing study

A full-thickness defect model was used to assess the healing efficiency of the hydrogels.<sup>52,53</sup> In brief, all rats were randomly divided into 9 groups: control, Alfa (available in the market), AGC, AGC-PPP, AGC-PRP, AGC-PPP-PDA (–NIR), AGC-PRP-PDA (–NIR), AGC-PPP-PDA (+NIR), and AGC-PRP-PDA (+NIR). The rats (male, 180 g) were anesthetized using ketamine/xylazine (6 : 4, v/v), and then 10 mm diameter full-thickness skin round wounds were created after shaving on the dorsal area of the rats. Then, the wounds were inoculated with 20  $\mu\text{L}$  of an *S. aureus* suspension ( $\sim 10^8$  CFU  $\text{mL}^{-1}$ ). The rats were subjected to the following different treatments. In the NIR groups, the wounds were irradiated with a NIR laser (808 nm, 1 W  $\text{cm}^{-2}$ ) after adding the hydrogels for 5 min and maintained at 42–45 °C. The regeneration process of wounds was evaluated by wound area monitoring. To monitor, the wounds were photographed on days 0, 5, 10 and 20. The wound dressings were replaced on day 2 and 5. The wound area was analyzed using ImageJ software. Wound closure performance for any treatment was assessed according to the formula:

$$\text{Relative wound size (\%)} = \text{Area}_n/\text{Area}_0 \times 100\%, \quad (16)$$

where  $\text{Area}_0$  and  $\text{Area}_n$  are the wound areas on day 0, and day 5, 10 or 20, respectively.

### 2.21 Ethical standards

All animals were housed in an animal room before starting the examination, allowing adaptation to the new environment. Principles of laboratory animal care were followed and the procedure was conducted in accordance with the ethical standards and protocols approved by the committee of animal experimentation guidelines of Zanjan University of Medical Sciences, Zanjan, Iran (ethical code: IR.ZUMS.REC.1400.071).

### 2.22 Histological analysis

Wound tissue samples were collected on the 5th, 10th, and 20th day for the histopathological study of epidermal regeneration and inflammation in the wound area. The samples were fixed in 10% neutral buffered formalin solution, dehydrated (using ascending alcohols), clarified with xylene, impregnated with melted paraffin, paraffin-embedded, and sectioned to 5  $\mu\text{m}$  thick slices, and finally, stained with hematoxylin and eosin (H&E) and Masson's trichrome. All samples were analyzed using a microscope and a Dino-Lite camera and using Dino-Capture software (V.2).

### 2.23 *In vivo* toxicity

The rats (male, 250 g) were randomly divided into 3 groups ( $n = 2$ ): AGC, AGC-PPP-PDA, and AGC-PRP-PDA groups. The rats were anesthetized using ketamine/xylazine (6 : 4, v/v). 200  $\mu$ L of sterilized AGC, AGC-PPP-PDA, and AGC-PRP-PDA hydrogels were injected subcutaneously under the rat's dorsal skin. After 7 and 21 days, the rats were sacrificed and the tissues were collected and embedded in 4% formaldehyde. The samples were monitored by H&E staining.

### 2.24 Statistical analysis

The experimental data were expressed as mean  $\pm$  standard deviation (SD). Statistical differences were analyzed using a general linear model, repeated measure design and one-way ANOVA, followed by the Bonferroni test for multiple comparisons using SPSS, version 25 (IBM). In all cases,  $p < 0.05$  was considered statistically significant.

## 3. Results and discussion

### 3.1 Fabrication and characterization of the hydrogels

The morphology of PDA NPs was identified by SEM (Fig. 2A and B). According to the SEM image, PDA NPs showed a uniform size of  $173.9 \pm 1.1$  nm with a spherical morphology. Zeta potential of the NPs was determined to be  $-21.3$  mV, which was similar to that in previously reported studies (Fig. S2†).<sup>54</sup> The cross-linking network AGC-PRP-PDA hydrogel was formed by blending of AGC-PRP-PDA polymeric solution and TBL +  $\text{CaCl}_2$  aqueous solution as a cross-linker (Fig. 2C). In addition, SEM was applied to observe the morphological features of the lyophilized hydrogels. As shown in Fig. 2D, a 3D structure with open pores was observed in the Alg-Ca hydrogel. The morphology of the AGC hydrogel became denser than Alg-Ca with the introduction of gelatin into the Alg-Ca network. PPP-Ca-TPL and PRP-Ca-TPL hydrogels presented an accumulation of irregular sheet-like fibrin fibers.<sup>3,55</sup> In contrast, AGC manifested a porous structure with a wide pore size distribution (Fig. 2D and F). After the introduction of PPP, PRP, and PDA, the porous network structure was retained, and the pore size distribution decreased. Additionally, a wider distribution of pores was observed in AGC-PPP-PDA compared to AGC-PRP-PDA. This can be attributed to the fact that the same volume of PRP and PPP was used in the preparation of the hydrogels. Our measurements showed that the amount of platelets was 3.8 times more in the case of the PRP fraction (Fig. S7†). Therefore, at the same volume, the larger pores were initially filled, thus resulting a noticeable decrease in the pore diameter and pore size distribution in AGC-PRP-PDA than AGC-PPP-PDA (Fig. 2F-H). Energy dispersive spectroscopy (EDS) analysis was employed to analyze the elements of the platelet-containing hydrogels. As shown, the sulfur element recognized in the AGC-PRP-PDA hydrogel, indicating the fibrin networks, could permeate inside the hydrogels, demonstrating successful fabrication of the hydrogels (Fig. 2E).<sup>55</sup> Collectively, the three-dimensional and porous structure of the

hydrogels can enhance the transmission of oxygen and nutrients, creating a moist environment, and can absorb wound secretions which are beneficial for wound repair.<sup>55–57</sup> Furthermore, the successful preparation of AGC, AGC-PRP-PDA, and AGC-PPP-PDA hydrogels was confirmed by FTIR through identifying the surface functional groups of the hydrogels (Fig. 3A). The peak at  $530\text{ cm}^{-1}$  in the AGC, AGC-PPP-PDA, and AGC-PRP-PDA hydrogel spectra is attributed to the metal-oxygen bond, which is considered as the key characteristic peak in the formation of the hydrogels.<sup>58</sup> Generally, the spectra of the pure compounds (GT, Alg, and  $\text{CaCl}_2$ ) broadened and shifted to higher wavenumbers after the fabrication of AGC, AGC-PPP-PDA, and AGC-PRP-PDA. For example, in the spectrum of calcium chloride hexahydrate, the absorption band at  $1630\text{ cm}^{-1}$  was due to the bending vibration of the H-O-H bond of crystal water.<sup>59</sup> In addition, a band at  $2900\text{ cm}^{-1}$  could be related to the C-H stretching vibrations of alginate.<sup>60</sup> Such absorption bands broadened and shifted to higher wavelengths in the spectra of AGC-PRP-PDA and AGC-PPP-PDA. These results demonstrated successful fabrication of the hydrogels through attractive interactions between the functional groups of the hydrogels by coordinative and hydrogen bonding interactions.<sup>7,17</sup> All of the hydrogels exhibited a high water content, which is essential in the wound repair process (Fig. 3B). The swelling profile of the AGC-PRP-PDA hydrogel was measured by gravimetric analysis (Fig. S3A†). The good swelling properties of AGC-PRP-PDA endow the hydrogels with capabilities to effectively maintain a wet environment during wound healing, absorb the exuded tissue, and control the release of bioactive materials such as growth factors.<sup>61,62</sup> An *in vitro* gel degradation assay was carried out in PBS (pH 7.4). As shown in (Fig. S3B†), degradation of AGC-PRP-PDA increased over time. The UV-vis-NIR absorbance spectra of AGC-PRP-PDA, AGC-PPP-PDA, and PDA showed absorbance in the NIR region (700–900 nm), demonstrating NIR activity of the materials, which is a crucial factor in PTT. As shown, this activity increased with increasing concentration, indicating that the photoactive properties of the materials were concentration-dependent (Fig. 3C and D).

### 3.2 Molecular docking study

The release of the trapped molecules in the hydrogel structure was determined by the various characteristics of the hydrogel at macroscopic and molecular scale levels. The interactions of drugs with polymeric chains of hydrogels such as hydrophobic and electrostatic attractions on an atomic scale play an important role in the sustained release of drugs.<sup>63,64</sup> In this study, to investigate the role of the molecular structure of the hydrogels in the slow release of growth factors, *i.e.*, VEGF and TGF- $\beta$  proteins, a molecular docking study was used to evaluate the interaction of alginate and gelatin as ligands with the proteins (Fig. 3E and F). The value of the binding energy of the best position for each run is presented in Table 1. The more negative binding energy values for all complexes indicate more affinity between the growth factor and alginate/gelatin ligands, resulting from favourable interactions between gelatin and



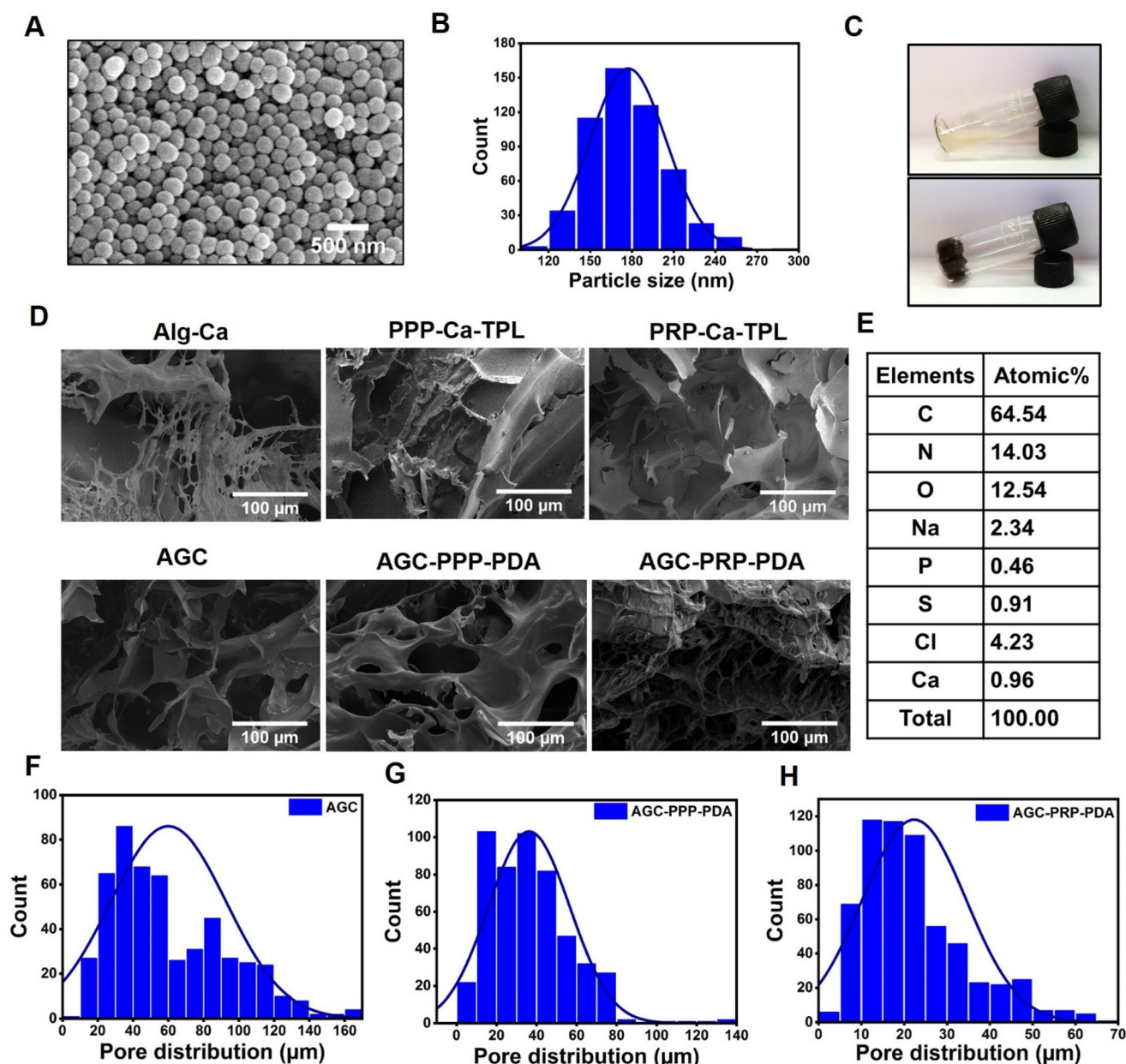


**Fig. 2** (A) SEM image of PDA NPs, scale bar: 500 nm. (B) Histogram distribution of PDA NPs. (C) Digital images of AGC (top image) and AGC-PRP-PDA (bottom image) hydrogels. (D) SEM image of the hydrogels. (E) EDS analysis of the AGC-PRP-PDA hydrogel. (F-H) Pore size distribution of the AGC, AGC-PPP-PDA, and AGC-PRP-PDA hydrogels, respectively.

alginate fragments with the neighboring amino acids at the binding site of the proteins. Our computational studies showed that VEGF had much higher affinity toward gelatin than the alginate segment. In contrast, TGF- $\beta$  exhibited high affinity toward the alginate fragment (Table 1).

### 3.3 Rheological performance

The mechanical properties of the hydrogels were evaluated by a rheology amplitude sweep test (Fig. 4). The results showed that the hydrogels had a gel-like behavior with the storage modulus ( $G'$ ) being higher than the loss modulus ( $G''$ ). The

addition of PPP and PRP did not significantly affect the rheological properties of the hydrogels, indicating that they were stable and had good consistency. Moreover, the viscosity of the hydrogels decreased with increasing shear rate, indicating their shear thinning properties, thus making the hydrogels to be injectable (Fig. 4E). The hydrogels also exhibited shear-thinning properties, which allowed them to be easily injected using a syringe (Fig. 4F).<sup>65,66</sup> In addition, we evaluated the rheological performance of AGC-PRP with/without PDA using a shear thinning assay of the hydrogels. As shown in Fig. S4A,† PDA did not affect the rheological behaviour of AGC-PRP.



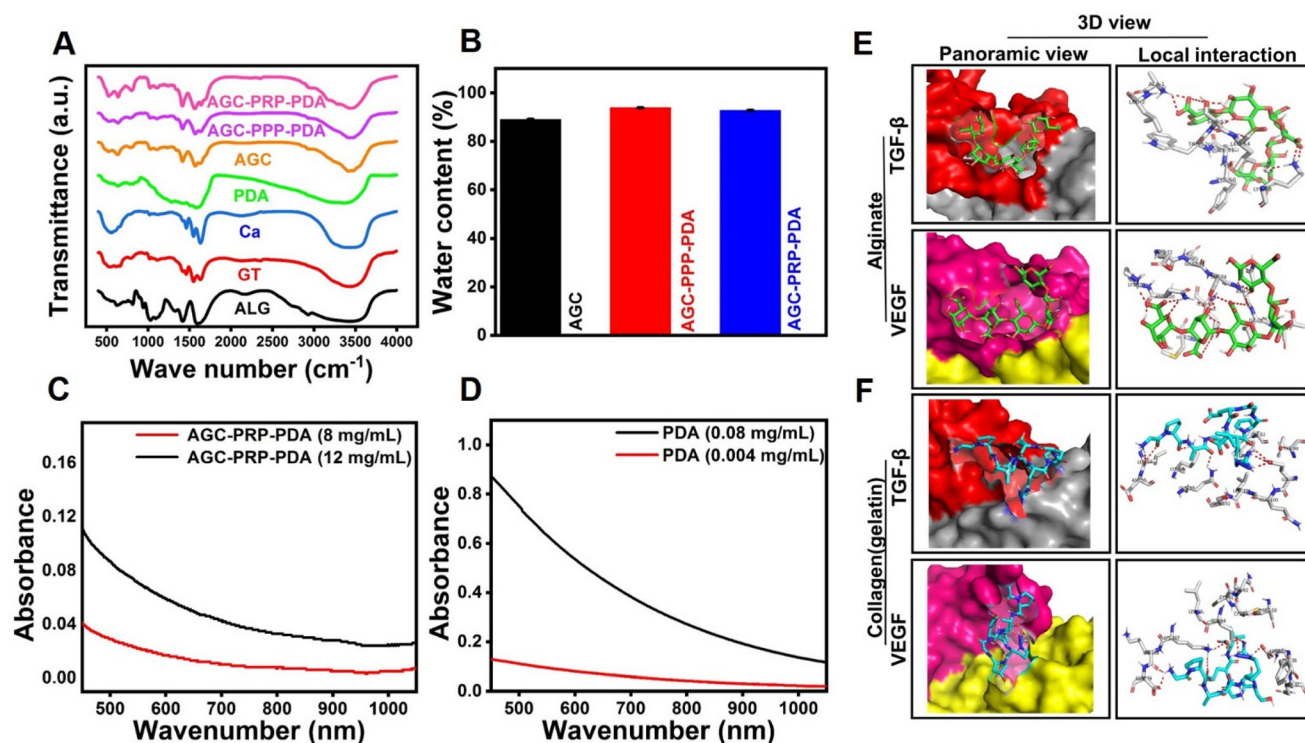


**Fig. 3** (A) FTIR spectra of the components of the AGC, AGC-PPP-PDA, and AGC-PRP-PDA hydrogels. (B) Water content of the hydrogels. (C and D) UV-vis-NIR spectra of PDA NPs and AGC-PPP-PDA hydrogels at different concentrations. (E and F) Structures of the complexes of growth factors with hydrogel polymers predicted by docking simulations. The panoramic images show the location of the alginate and collagen (gelatin) fragments on the surface of TGF- $\beta$  and VEGF. The local interaction images represent the hydrogen bonds between polymers and amino acids surrounding the binding site of the growth factors.

**Table 1** Binding energy of the top-ranked docking poses for growth factors complexed with hydrogel polymers

| Ligand/target         | Binding energy (kcal mol <sup>-1</sup> ) |
|-----------------------|------------------------------------------|
| Alginate/VEGF         | -0.2                                     |
| Alginate/TGF- $\beta$ | -5.21                                    |
| Gelatin/TGF- $\beta$  | -4.01                                    |
| Gelatin/VEGF          | -5.80                                    |

### 3.4 Photothermal properties of the hydrogels

PTT has been extensively developed as an effective and safe method for bacterial elimination through heat generation from NIR light absorption.<sup>34,67</sup> PDA acted as a photothermal agent in the AGC-PRP-PDA hydrogel. As shown in Fig. 5A, the hydrogel without PDA (AGC-PRP) indicated no significant temperature change. The *in vitro* photothermal effect of the AGC-PRP-PDA hydrogel was examined at various amounts of PDA (5  $\mu$ L and 10  $\mu$ L, 5 mg mL<sup>-1</sup>) and different power densities for 10 min under NIR laser irradiation. As shown in Fig. 5B and C, the temperatures increased with increasing concentration and power densities. Photothermal stability of the hydrogel was investigated by exposing the hydrogels to five heating/cooling cycles (Fig. 5D). The thermal performance of the AGC-PRP-PDA hydrogel showed no difference during the five cycles of NIR irradiation and free cooling continuous illu-

mination, indicating good photostability of the hydrogel. Additionally, the photothermal conversion efficiency ( $\eta$ ) was measured by obtaining the value of  $\tau_s$  ( $\tau_s = 297.27$ ).<sup>68,69</sup> The  $\eta$  value of the AGC-PRP-PDA hydrogel was calculated to be 18.2% (Fig. 5E and F, and eqn (2)). The infrared thermographic image of the AGC-PRP-PDA hydrogel was recorded by NIR laser irradiation (808 nm, 1 W cm<sup>-2</sup>) (Fig. 5G and H). After 10 min of irradiation, there was no noticeable temperature increase for the hydrogel without PDA just at about 4.5 °C, whereas the temperature of the hydrogel with PDA increased instantaneously by 24 °C. We also observed that the photothermal activity of AGC-PRP-PDA and AGC-PPP-PDA hydrogels was similar (data are not shown).

### 3.5 NIR-assisted antibacterial properties of the hydrogels

The essential factor in wound repair is the inhibition of bacterial infection.<sup>5,39,41</sup> The antibacterial activity of the hydrogels was tested against the Gram-negative and Gram-positive bacterial strains in the presence and absence of 808 nm NIR light. Normal saline and the AGC hydrogel were taken as the control groups (Fig. 6). When introducing PDA as a photothermal agent, the AGC-PPP-PDA and AGC-PRP-PDA hydrogels showed a considerably decreased bacteria survival ratio of 22.88% for *E. coli* and 37.34% for *S. aureus*, and 29.16% for *E. coli* and 18.38% for *S. aureus*, respectively. In contrast, the

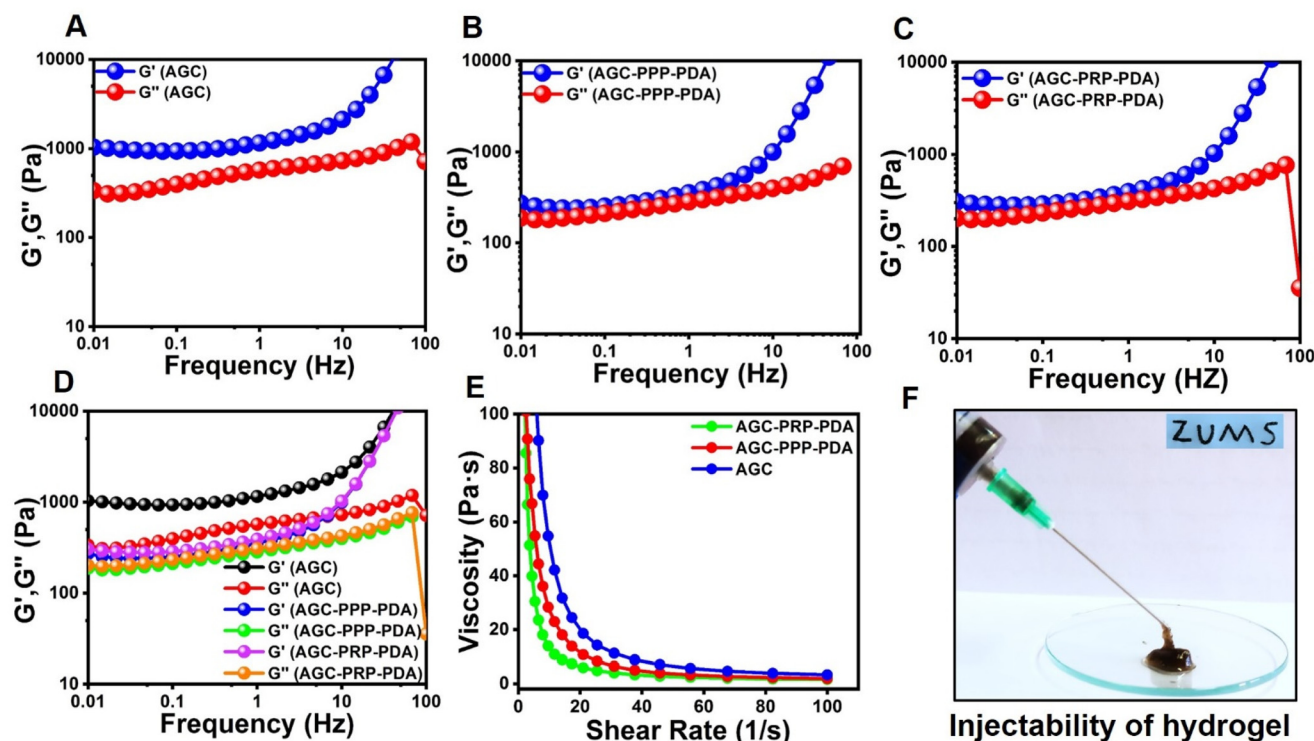


Fig. 4 Rheological performance of the hydrogels. (A) Frequency sweep test of (A) AGC, (B) AGC-PPP-PDA, and (C) AGC-PRP-PDA hydrogels. (D) Rheological performance of the hydrogels determined by employing an oscillation–frequency test. (E) Shear thinning assay of the hydrogels. (F) Injectability test of the AGC-PPP-PDA hydrogel using a 27-G needle.

bacteria survival ratio of these hydrogels without NIR light for *E. coli* and *S. aureus* had not been reduced compared to the control group. There were no obvious change in the colonies in the control group with or without NIR light. According to Fig. 6B–D, no bacterial killing occurred in the AGC hydrogel group both in the presence/absence of NIR irradiation. Furthermore, the antibacterial performance of PDA NPs was tested against *E. coli* and *S. aureus* based on the photothermal ability in LB broth medium (Fig. S5†). It has been reported that bacterial strains can be killed during PTT when the temperature is increased to 45 °C.<sup>24,67,70</sup> The generated heat could cause destruction of bacteria by damage to the cellular membrane and intracellular proteins.<sup>39,71,72</sup>

### 3.6 Antioxidant properties of the hydrogels

There is a high amount of ROS produced through oxidative stress at a wound site, thus resulting oxidation of proteins and lipids, or DNA damage.<sup>73</sup> Therefore, design and fabrication of multifunctional wound dressings with antioxidant properties is of particular importance. Free radical scavenging capacity of PDA has been reported related to the catechol-rich surface of PDA and their quinone groups.<sup>9,74–76</sup> As shown in Fig. 6F, the visible spectroscopy of the DPPH solution showed an obvious absorption at 517 nm. The indicator was a stable RNS compound and its ethanol solution color was purple.<sup>42</sup> The decolorization of DPPH in AGC, AGC-PPP-PDA, and AGC-PRP-PDA solutions is shown in Fig. 6G. When the DPPH solution was exposed with AGC-PPP-PDA and AGC-PRP-PDA disper-

sions, the color of the solutions was completely faded and there was no absorbance peak at 517 nm, indicating reduction of DPPH by the hydrogels (Fig. 6F and G). Furthermore, the DPPH scavenging performance of the AGC-PRP-PDA hydrogel indicated a concentration-dependent behaviour. The DPPH scavenging ratio increased from 38% to 86% when the amount of the AGC-PRP-PDA hydrogel increased from 2 mg to 5 mg (Fig. 6H and I). In another attempt, the antioxidant properties of the AGC-PRP-PDA hydrogel were assessed using salicylic acid as an indicator.<sup>77</sup> As shown in Fig. 6J, the absorption peak of salicylic acid disappeared upon using the AGC-PRP-PDA hydrogel at 517 nm. On the other hand, this effect was promoted with increasing concentration of the hydrogel. In addition, excellent H<sub>2</sub>O<sub>2</sub> scavenging properties were found upon using AGC-PRP-PDA (Fig. S6†). We used ascorbic acid as a positive antioxidant agent. At a lower concentration (6 mg mL<sup>−1</sup>), the scavenging percentage was similar to that of ascorbic acid, while at a higher concentration (10 mg mL<sup>−1</sup>), the H<sub>2</sub>O<sub>2</sub> scavenging activity (%) of AGC-PRP-PDA was significantly higher than ascorbic acid (*P* < 0.01). The above results demonstrated that the existence of PDA endowed the hydrogel with excellent antioxidant properties, thus, highlighting the potential application of the antioxidant hydrogels for skin wound regeneration.<sup>39</sup>

### 3.7 In vitro cytotoxicity and biocompatibility evaluations

A desirable wound dressing should possess hemostatic capacity with good hemocompatibility.<sup>35,78</sup> Hemocompatibility

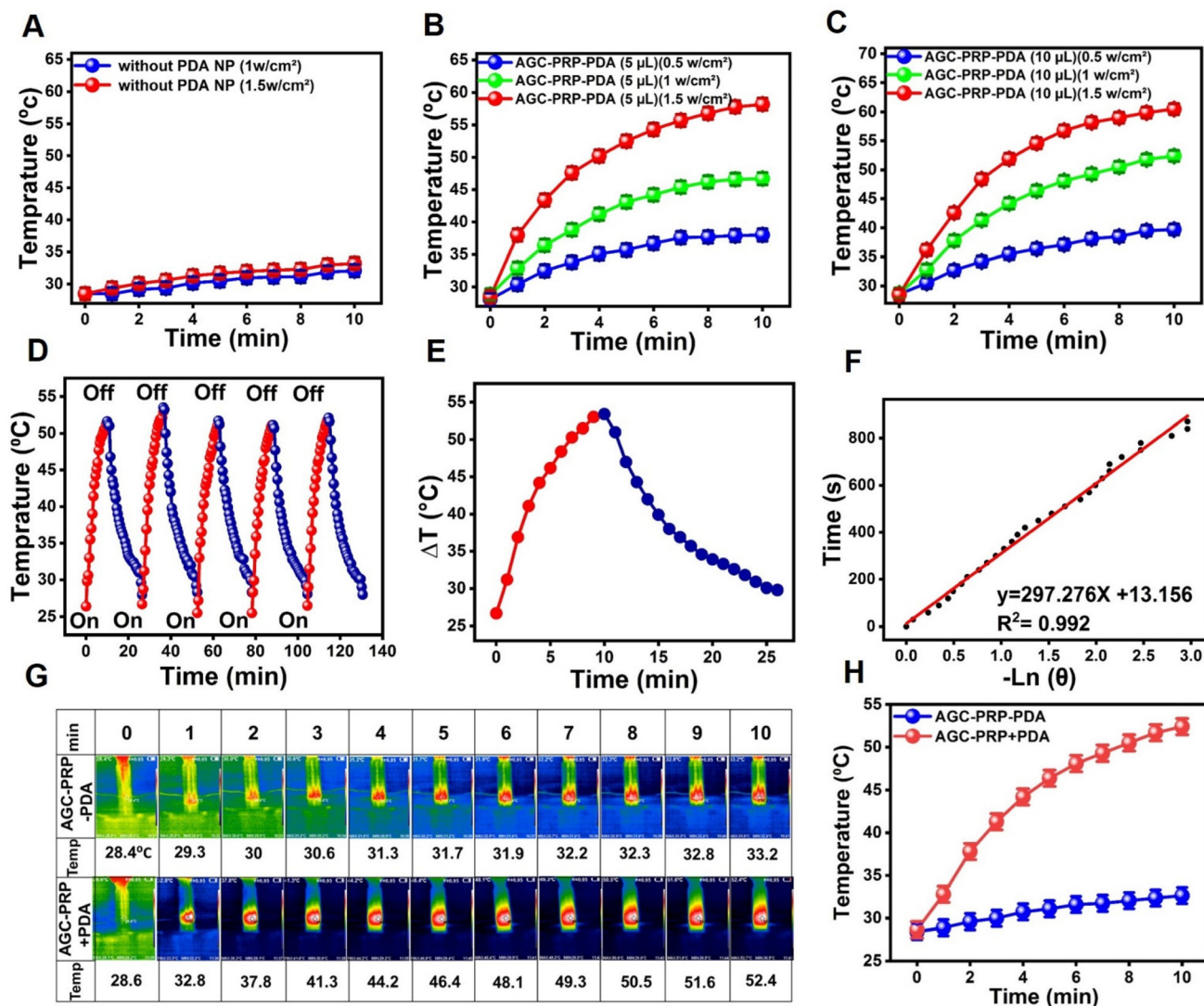


**Fig. 5** (A) Temperature elevation of the AGC-PRP hydrogel at different powers of NIR light (808 nm). (B and C) Temperature increase profiles of the AGC-PRP-PDA hydrogel at different concentrations and powers over 10 min. (D) Temperature changes of AGC-PRP-PDA during five on/off cycles of NIR laser illumination at  $1.0 \text{ W cm}^{-2}$  for 130 min. (E) Photothermal response of the AGC-PRP-PDA hydrogel for one cycle using a 808 nm laser ( $1 \text{ W cm}^{-2}$ ). (F) Linear time data versus  $-\ln \theta$  measured using the cooling period. (G and H) Infrared thermal images and the temperature profile of the AGC-PRP-PDA hydrogel under 808 nm laser irradiation ( $1 \text{ W cm}^{-2}$ ) (mean  $\pm$  SD,  $n = 3$ ).

of AGC, AGC-PPP-PDA, and AGC-PRP-PDA hydrogels was investigated by a hemolysis test (Fig. 7A–D). As shown, all of the hydrogels showed a negligible hemolysis ratio ( $<2.5\%$ ), exhibiting excellent hemocompatibility *in vitro*. In the hemolytic test, deionized water (positive control group) showed an apparent red color, while the hydrogel groups showed the same color as PBS (negative control group) (Fig. 7D). Cytocompatibility evaluation is an essential factor for any biomaterial to be used in biomedical applications (Fig. 7E and F).<sup>56,79,80</sup> Fibroblast cells plays a main role in the wound healing process and their proliferation and migration accelerate wound closure.<sup>68,81</sup> Cytocompatibility of the hydrogels was examined with NIH3T3 fibroblast cells using an MTT assay.

During co-incubation for 48 and 72 h, all groups had higher than  $\sim 90\%$  cell viability even at a concentration of  $1 \text{ mg}$

$\text{mL}^{-1}$ , indicating cytocompatibility of the hydrogels. Such findings demonstrated that all the hydrogels had desirable hemocompatibility and cytocompatibility, making them excellent candidates for subsequent wound regeneration.

### 3.8 Hemostatic performance of the hydrogels

During an injury in the skin, bleeding is unavoidable. Therefore, evaluation of hemostasis should be the first stage in the wound repair assessment.<sup>82</sup> *In vitro* blood clotting properties of the hydrogels and gauze were measured using the whole blood-clotting index three times (60, 120, and 240 s) at  $37^\circ\text{C}$ .<sup>7</sup> Gauze as a traditional hemostatic model was used as the control. Both AGC-PPP-PDA, and AGC-PRP-PDA groups indicated a lower BCI than the control group and no significant difference between the AGC-PPP-PDA and AGC-PRP-PDA



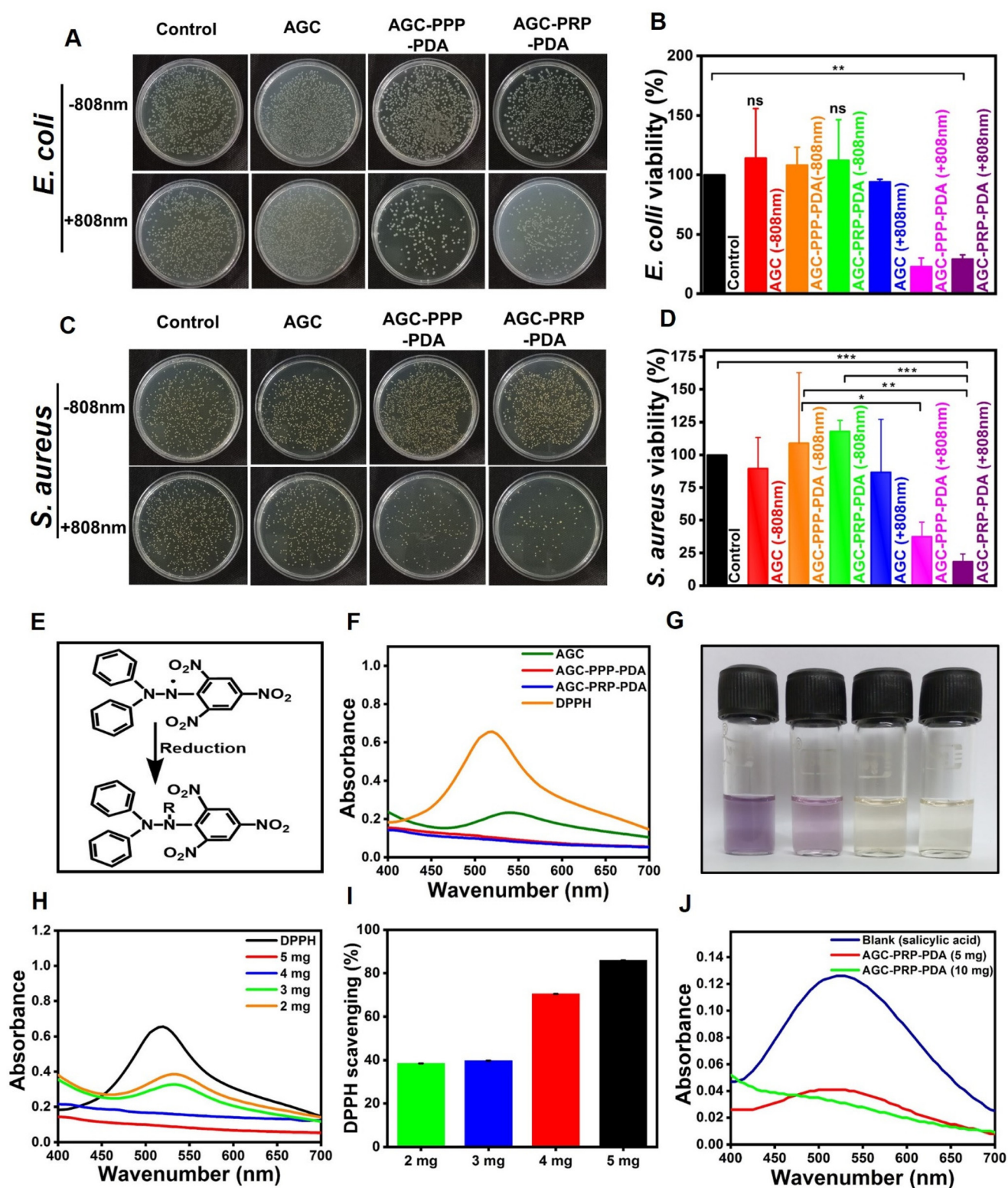


**Fig. 6** Illustration of the antibacterial activity of the hydrogels with and without NIR light. (A) Image of the agar plate indicating *E. coli* growth. (B) Viability ratio of *E. coli*. (C) Image of the agar plate indicating *S. aureus* growth. (D) Viability ratio of *S. aureus* growth of the hydrogels with and without NIR light (mean  $\pm$  SD,  $n = 3$ ,  $*p < 0.05$ ,  $**p < 0.01$ ). Antioxidant performance of the hydrogels. (E) Reduction mechanism of DPPH. (F) Absorbance curve of different hydrogels and DPPH. (G) Digital images of DPPH and the hydrogel solutions. (H) Absorbance spectra of different amounts of the hydrogels and DPPH. (I) Scavenging rate of different amounts of the hydrogels. (J) Antioxidant activity of the AGC-PRP-PDA hydrogel with salicylic acid.



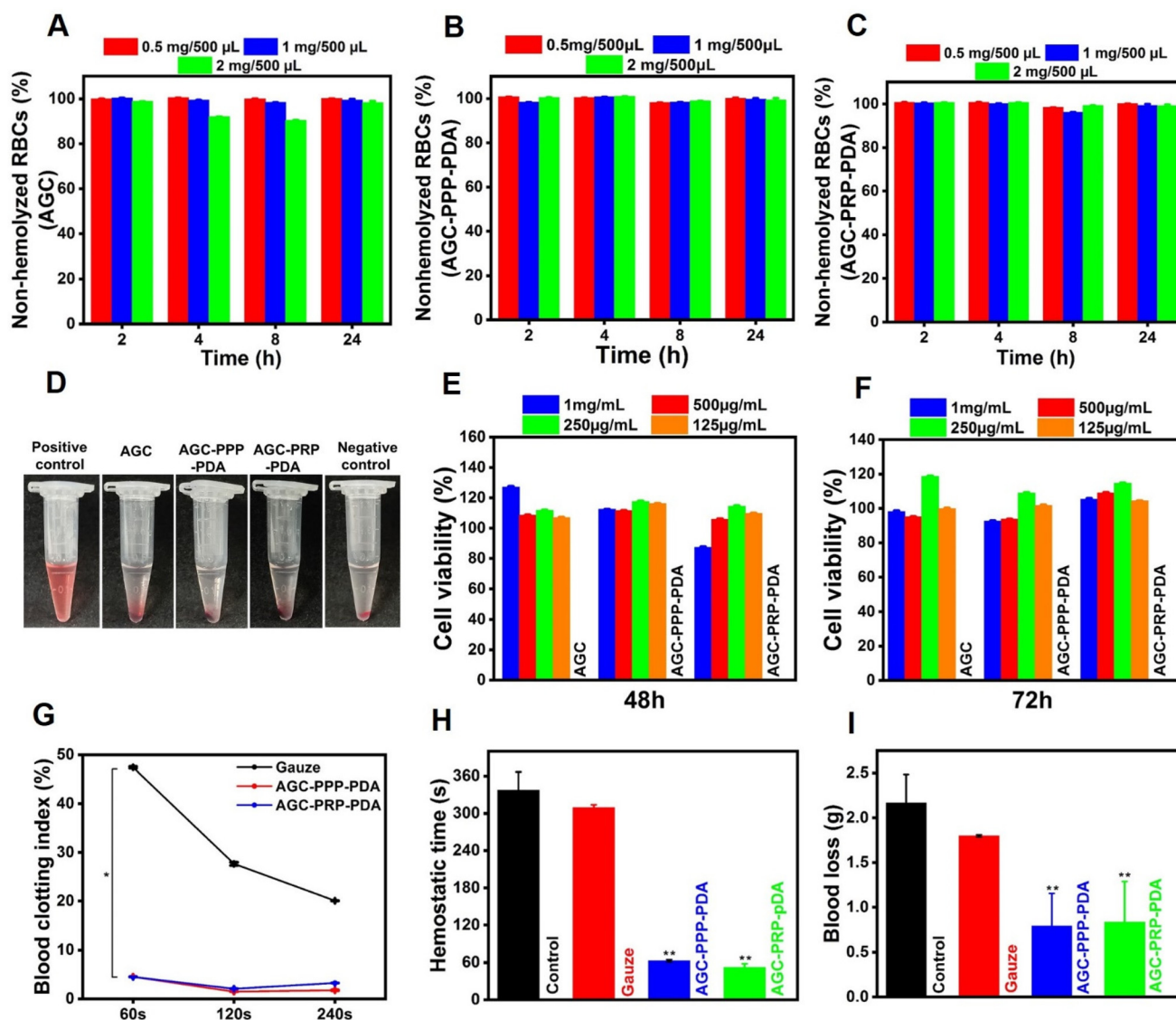


**Fig. 7** Biocompatibility evaluation and hemostatic performance of the hydrogels. *In vitro* cell viability assays of (A) AGC, (B) AGC-PPP-PDA, and (C) AGC-PRP-PDA hydrogels at different concentrations. (D) Images of the supernatants of RBC suspensions treated with deionized water, the hydrogels, and PBS (pH  $\sim$  7.4). Cell viability evaluation of the hydrogels at (E) 48 h and (F) 72 h (mean  $\pm$  SD,  $n$  = 3, \* $p$  < 0.05, \*\* $p$  < 0.01). (G) *In vitro* BCI index of the hydrogels, gauze, and control groups after 60, 120, and 240 s. (H and I) *In vivo* hemostatic time blood loss evaluation in a wound tail amputation model for the different groups (mean  $\pm$  SD,  $n$  = 3, \* $p$  < 0.05, \*\* $p$  < 0.01).

groups was observed (Fig. 7G). When the AGC-PRP-PDA or AGC-PPP-PDA hydrogels were placed as powder for wound tail amputation, blood loss was quickly stopped at 52 and 63 s, respectively; the timings were significantly shorter than those of the control group (337 s), confirming a promising performance of the hydrogels as a hemostatic agent (Fig. 7H). In addition, the *in vivo* hemostatic properties of the hydrogels were further evaluated by the amount of blood loss in the model. Total blood loss in the control group (without treatment) was calculated to be 2.1 g in 337 s. In contrast, the amount of blood loss was  $\sim$ 1 g in the AGC-PRP-PDA and AGC-PPP-PDA hydrogel-treated groups at 52 and 63 s, respectively (Fig. 7H and I). Hemostatic images under different treat-

ments also clearly showed the anti-bleeding properties of the hydrogels (Fig. S8†). On one hand, the hemostasis capacity of the hydrogels in the tail amputation model might be related to the strong adhesiveness between the amputated tail and the PDA-containing hydrogels acting as a physical barrier for bleeding. PDA has catechol groups, endowing the material with high adhesive properties. Therefore, wound dressings containing PDA possess enhanced adhesiveness to a wounded tissue, thus improving the hemostatic effect of the dressing.<sup>39</sup> On the other hand, the hemostatic function of platelets endows AGC-PRP-PDA and AGC-PPP-PDA hydrogels with anti-bleeding properties to promote hemostasis immediately after the injury.<sup>33</sup> Therefore, the abovementioned properties

introduced the multifunctional hydrogels as a good candidate in wound closure for their excellent anti-bleeding performance.

### 3.9 *In vitro* growth factor release evaluation

VEGF and TGF- $\beta$  play an important role for promoting wound healing. VEGF is a key dynamic molecule stimulating angiogenesis. In addition, it is involved in the migration process of fibroblast cells to accelerate wound closure.<sup>30,83</sup> TGF- $\beta$  regulates not only angiogenesis, inflammation, and granulation tissue formation, but also re-epithelialization, thus accelerating the healing process.<sup>84</sup> The rapid release of growth factors from PRP limits its clinical applications.<sup>3</sup> In order to achieve a sustained release of growth factors, loading PRP into a hydrogel is a promising strategy to improve wound healing efficiency.<sup>56,57,85</sup> An ELISA assay was used to evaluate the release curves of VEGF and TGF- $\beta$  (Fig. 8A and B). As shown, the burst release of the PRP gel (without Alg, the gel, and the cross-linker) was realized in the initial hours, while the release behaviours of VEGF and TGF- $\beta$  were relatively slower, indicating better sustained release properties of the growth factors in the AGC-PRP-PDA hydrogel compared to the PRP gel.

### 3.10 *In vitro* wound healing assay

To evaluate whether the AGC-PRP-PDA hydrogel could promote the migration of repaired cells, a scratch assay was performed using NIH3T3 cells. The *in vitro* test is a well-known method based on creating a “scratch” on a cell monolayer mimicking to some extent cell-cell and cell-matrix interactions during wound healing *in vivo*.<sup>86</sup> The results showed that the proliferation of NIH3T3 cells was stimulated by AGC-PRP-PDA and AGC-PPP-PDA hydrogels faster than the control (without treatment) group (Fig. 8C). After 24 h, the relative wound areas in the AGC-PRP-PDA, AGC-PPP-PDA hydrogels and control group were determined to be 11%, 24.8%, and 55.5%, respectively (Fig. 8D). As shown, compared with AGC-PRP-PDA, the *in vitro* wound healing was significantly higher than AGC-PPP-PDA. This can be attributed to the higher expression of growth factors in the case of AGC-PRP-PDA, thus accelerating the repair of the scratch area effectively.<sup>26,87</sup> For example, it has been shown that the platelet derived growth factors such as VEGF could regulate cell proliferation and migration.<sup>88</sup> Moreover, we measured the amount of platelets at similar volumes of PRP and PPP fractions. The amount was 3.8 times more in the case of the PRP fraction (Fig. S7†). It should be noted that gelatin can promote cell adhesion and proliferation, thus accelerating wound closure.<sup>14</sup> These results show that PRP/PPP-loaded hydrogels could stimulate fibroblast growth, suggesting the possibility of prompting the wound healing process *in vivo*.

### 3.11 *In vivo* wound healing study

The PRP-loaded hydrogels presented sustained release of growth factors and exhibited excellent photothermal antibacterial activity as well as improved cell migration behaviors in our *in vitro* studies. The therapeutic efficiency of the hydrogels

was evaluated using an infected wound model. We established a 10 mm diameter full-thickness skin wound on the back of rats, followed by infecting the wound site using *S. aureus* ( $\sim 10^8$  CFU mL<sup>-1</sup>). Except for the control group (no treatment), wounds were covered by the hydrogels and monitored on days 5, 10, and 20 during the healing process. Alfa ointment (available in the market) was used for the control group (Fig. 9A). Compared with the other groups, the AGC-PRP-PDA (+NIR) treated group showed a faster wound closure rate. Quantitative wound closure results are shown in Fig. 9E. On day 5, the AGC-PRP, AGC-PRP-PDA ( $\pm$ NIR) and AGC-PRP-PDA ( $\pm$ NIR) groups healed significantly faster than the other groups ( $p < 0.05$ ) and statistical analysis suggested that there was no significant difference among the control, Alfa, and AGC groups. On days 10 and 20, wound closure occurred at both times and there was no significant difference among the groups on each day (Fig. 9C–E). The increased healing in AGC-PRP-PDA ( $\pm$ NIR) than the control group can be attributed to the antioxidant, antibacterial, and healing properties of the Alg-Gel-based hydrogels as well as the maintenance of a wet environment during wound healing by the hydrogel. *In vivo* antibacterial properties of AGC-PRP-PDA ( $\pm$ NIR) and AGC-PRP-PDA (+NIR) hydrogels were evaluated and the corresponding results are shown in Fig. 9F. The anti-infective effects were assessed by comparing the bacterial counts in the infected wounds. After 24 h of treatment, the control (without any treatment) and the AGC-PRP-PDA ( $\pm$ NIR) groups indicated a large number of surviving bacteria on the plate. In contrast, the AGC-PRP-PDA (+NIR) hydrogel showed a noticeable reduction in the bacteria number, providing a promising goal to use it as an excellent dressing to treat *S. aureus*-infected wounds (Fig. 9F). This finding highlighted the antibacterial activity of the hydrogel under NIR light irradiation stemming from PDA.<sup>39,89</sup> Fig. 9G shows the infrared thermal images of the treated groups with AGC-PRP-PDA under 808 nm laser irradiation (1 W cm<sup>-2</sup>).

As shown, the temperature at the wound site rapidly increased to 42 °C for 5 min, indicating the excellent photothermal activity of the hydrogel *in vivo* (Fig. 9G).

### 3.12 Histological analysis

To further evaluate the quality of the regenerated skin, H&E and Masson's trichrome staining on day 5, day 10, and day 20 were performed (Fig. S10†). As shown in Fig. 10A, after 5 days of the treatment, all groups indicated varying degrees of inflammatory cells, indicating the typical first stage of the wound repair process. New blood vessels are essential for wound healing, to provide nutrients and oxygen to the damaged area.<sup>39,90,91</sup> On day 5, the AGC-PPP-PDA (+NIR) and AGC-PRP-PDA (+NIR) groups exhibited more blood vessels than the other groups. On day 10, the AGC-PRP-PDA (+NIR) and AGC-PRP-PDA ( $\pm$ NIR) groups were covered with a thin layer of epithelial tissue. The AGC-PPP-PDA (+NIR) and AGC-PPP-PDA ( $\pm$ NIR) groups exhibited partial re-epithelialization on the edge of the wound. In addition, PRP-loaded hydrogels showed less inflammatory cell infiltration at the wound site

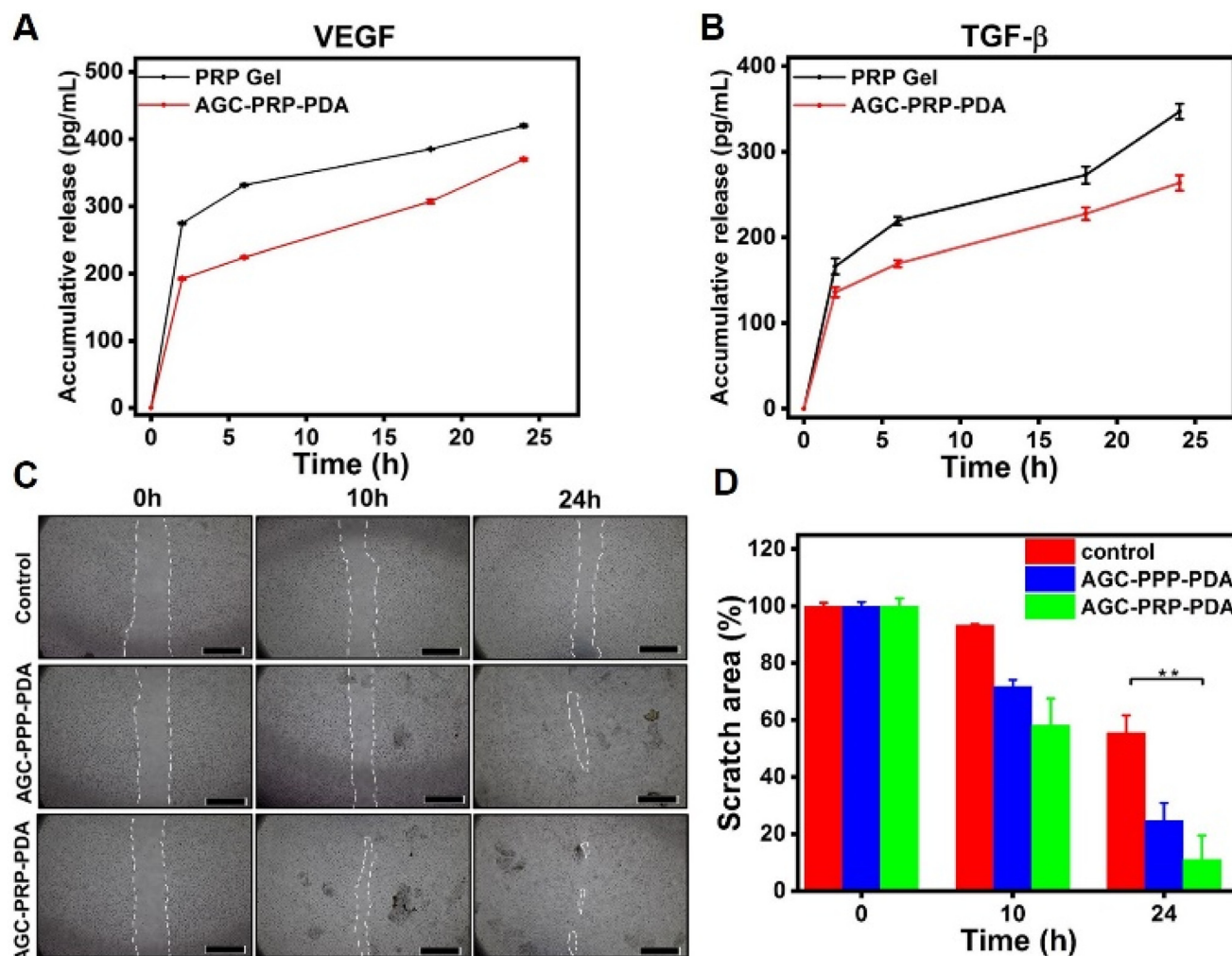


Fig. 8 Release profiles of (A) VEGF and (B) TGF- $\beta$  from the PRP gel and AGC-PRP-PDA hydrogel (mean  $\pm$  SD,  $n = 3$ ). *In vitro* wound healing (scratch assay) of the AGC-PPP-PDA and AGC-PRP-PDA hydrogels, and (C) the scratch image of NIH3T3 cells. (D) Relative healing area obtained for the hydrogel and control groups (mean  $\pm$  SD,  $n = 3$ , \*\* $p < 0.01$ ), scale bar: 1 mm.

than the PPP-loaded ones. However, no obvious epithelialization was observed for the other groups (Fig. 10B). On day 20, the wound in the AGC-PRP-PDA (+NIR) group reached the state of normal skin structure, and many skin accessory structures including mature blood vessels, hair follicles, and dermis thickening were observed in the group than the AGC-PRP-PDA (-NIR) group (Fig. S9†). Furthermore, it was observed that the epithelial thickness of the AGC-PRP-PDA groups at day 20 was reduced compared with the AGC-PPP-PDA groups, indicating a transition from phase three (proliferation) to phase four (remodeling) of a healing process (Fig. 10C).<sup>92</sup> Masson's trichrome staining was used to track collagen deposition throughout the wound repair process on day 20 (Fig. 10D). As shown, no obvious difference in collagen deposition was observed among the control, Alfa, AGC, AGC-PPP, and AGC-PRP groups. In addition, number of collagen fibers in the PRP- and PPP-containing groups was much higher when NIR light was used, confirming that collagen

deposition was improved by hyperthermia during the PTT. Compared with AGC-PPP-PDA (+NIR), well-arranged collagen deposition with dense fibers was observed in the AGC-PRP-PDA (+NIR) treated group, indicating the impact of the release growth factors in the healing process, which was more in the AGC-PRP-PDA group. These results demonstrated that AGC-PRP-PDA (+NIR) would be a promising hydrogel dressing for cutaneous tissue remodeling and regeneration.

### 3.13 *In vivo* biosafety evaluation of the hydrogels

*In vivo* biocompatibility is of vital importance for the hydrogels applied in regenerative medicine.<sup>67</sup> Biocompatible properties of AGC, AGC-PPP-PDA, and AGC-PRP-PDA hydrogels were evaluated by subcutaneous injection of the hydrogel into the shaved dorsal side of a male rat (Fig. 10E). The results were assessed by H&E staining on day 7 and day 21. On both days, epidermis, dermis, and hypodermis were similar to the natural skin. As shown in H&E images, inflammation was not



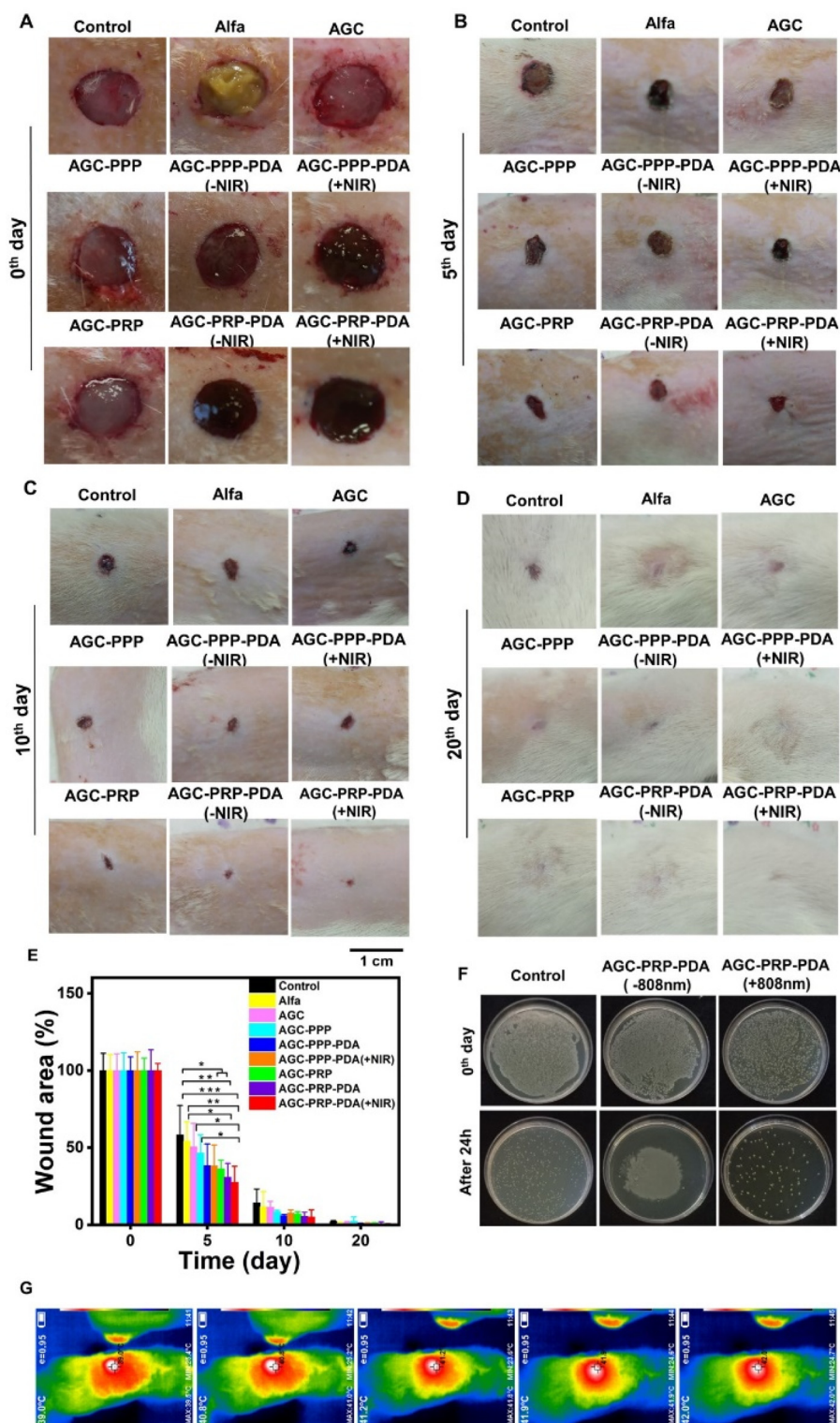


**Fig. 9** *In vivo* skin regeneration and antibacterial assay of the hydrogels. Macroscopic view of the wounds on (A) 0th, (B) 5th, (C) 10th and (D) 20th days. (E) Statistical wound closure ratio of all groups (mean  $\pm$  SD,  $n = 5$ ,  $*p < 0.05$ ,  $**p < 0.01$ ,  $***p < 0.001$ ). (F) *In vivo* antibacterial properties of AGC-PRP-PDA with and without NIR light irradiation after 24 h of treatment. (G) *In vivo* infrared thermal images of the wounds covered by the AGC-PRP-PDA hydrogel under 808 nm (1 W cm<sup>-2</sup>), scale bar: 1 cm.

observed and hair follicles were visible. In addition, fibroblasts and fibrocytes were the main connective cells. These findings indicated biocompatibility of the hydrogels. Moreover, the

histological analysis of the major organs (kidneys, livers, and spleens) in the AGC-PRP-PDA (+NIR)-treated group was used to further evaluate the biocompatibility of the hydrogel. As



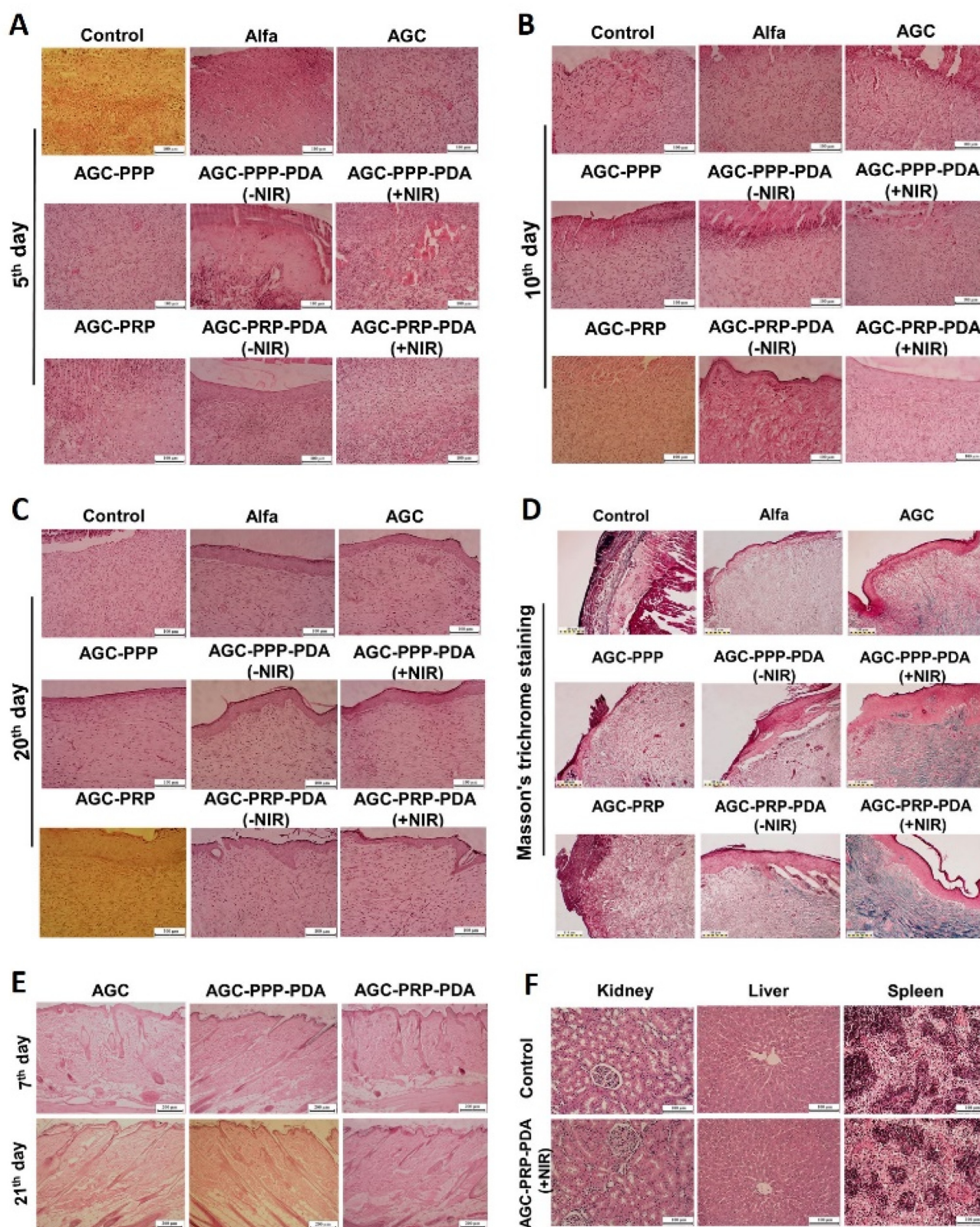


**Fig. 10** Histological analysis of the wound area with H&E staining after the (A) 5th, (B) 10th, and (C) 20th day of therapy for all groups, scale bar: 200  $\mu$ m. (D) Masson's trichrome staining histological images on day 20 for all groups, scale bar: 110  $\mu$ m. *In vivo* biocompatibility and biosafety assessment. (E) H&E staining image of the skin tissues after subcutaneous implantation on days 7 and 21. Scale bar: 200  $\mu$ m. (F) Histological evaluation of the kidneys, livers and spleens of the control and AGC-PRP-PDA groups. Scale bar: 100  $\mu$ m.

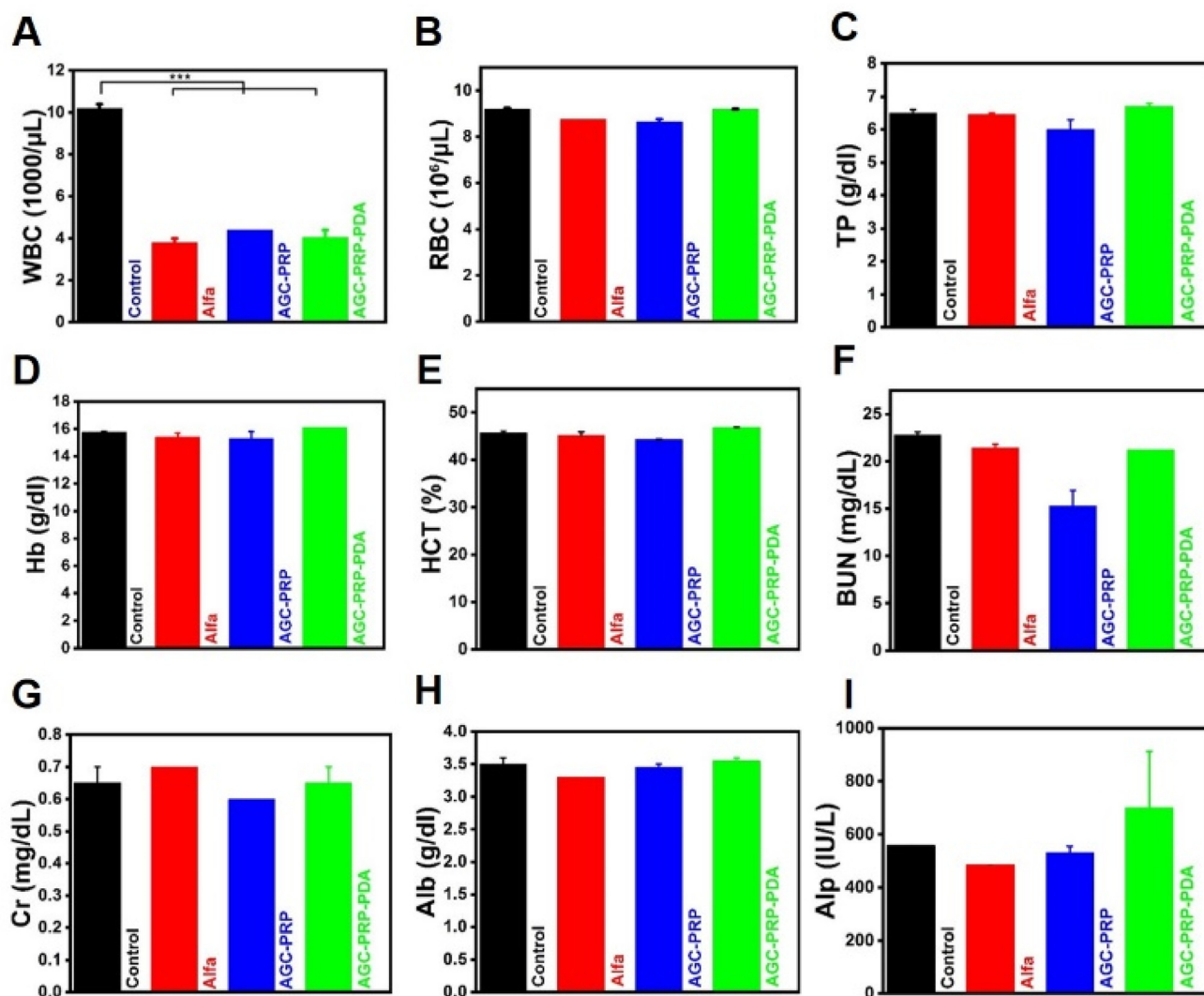


Fig. 11 Hematology and blood biochemical analysis of (A) WBCs, (B) red blood cells (RBCs), (C) blood platelets (PLT), (D) blood urea nitrogen (BUN), (E) creatinine (CRE), (F) lactate dehydrogenase (LDH), (G) haemoglobin (HGB), (H) alkaline phosphatase (Alp), and the (I) hematocrit test (HCT) for the control, Alfa, AGC-PRP, and AGC-PRP-PDA groups (mean  $\pm$  SD,  $n = 2$ , \*\*\* $p < 0.001$ ).

shown in Fig. 10F, no obvious pathological abnormalities or inflammation was observed in the treatment group.

Hematology and blood biochemical analysis were used to further evaluate the biosafety of the treatment groups (control, Alfa, AGC-PRP, and AGC-PRP-PDA) on day 20. As shown in Fig. 11A, the white blood cell (WBC) level in the control group was much higher than those of the Alfa, AGC, and AGC-PRP-PDA groups. This is because WBCs are involved in inflammatory responses and their amount are usually used as an index in the evaluation of inflammatory activities.<sup>24</sup> In addition, there were no significant differences in red blood cells (RBCs), total protein (TP), hemoglobin (HGB), hematocrit test (HCT), and renal function parameters [blood urea nitrogen (BUN) and creatinine (CRE)], as well as liver function parameters [albumin (Alb) and alkaline phosphatase (Alp)] between the control group and the Alfa, AGC, and AGC-PRP-PDA groups.

These findings confirmed good *in vivo* biocompatibility of the hydrogels.

## 4. Conclusion

Overall, this study highlights the potential of PRP-loaded hydrogels as a promising approach for the treatment of infected full-thickness skin defects. The combination of Alg and gelatin provided a stable and shear-thinning hydrogel with inherent photothermal effects, while the addition of PRP allowed for sustained release of growth factors to promote cell proliferation and angiogenesis. The hydrogel also demonstrated excellent biocompatibility, hemostatic effects, antioxidant properties, and antibacterial activity, making it a multifunctional wound dressing. In a mouse-tail amputation



model, the photothermally active AGC-PRP-PDA hydrogel significantly accelerated the healing process of full-thickness skin defects infected by *S. aureus*. These findings have important implications for the design of novel bio-photoactive injectable hydrogels for wound healing and skin reconstruction.

## Author contributions

Vajihe Alinezhad carried out the experiments with the support from Hadi Bagheri and Kimia Esmaeilzadeh. Habib Zeighami supervised the antibacterial studies. Rahim Jafari and Kimia Esmaeilzadeh performed the computational analysis. Pooyan Makvandi performed SEM and rheological analysis. Ali Kalantari-Hesari carried out the histopathological analysis. Yi Xu, Hamid Reza Mohammadi, and Mohammad-Ali Shahbazi revised the manuscript. Aziz Maleki directed and designed the project.

## Conflicts of interest

There are no conflicts to declare.

## Acknowledgements

This work was supported by the Zanjan University of Medical Sciences (Grant No. A-12-1143-5 and A-12-1291-6).

## References

- 1 F. Z. Amourizi, A. Z. Malek-Khatabi and R. Zare-Dorabei, *Mater. Chem. Horiz.*, 2023, DOI: [10.22128/MCH.2023.645.1036](#).
- 2 G. Heidari, M. Hassanpour, F. Nejaddehbashi, M. R. Sarfjoo, S. Yousefiasl, E. Sharifi, A. Bigham, T. Agarwal, A. Borzacchiello and E. Lagreca, *Mater. Chem. Horiz.*, 2022, **1**, 35–48.
- 3 J. Tang, H. Li, H. Peng, Z. Zhang, C. Liu, Y. Cheng, K. Wang, Z. Yu, Z. Lyu and J. Zhang, *Mater. Today Bio*, 2022, **17**, 100498.
- 4 H. N. Wilkinson and M. J. Hardman, *Open Biol.*, 2020, **10**, 200223.
- 5 A. Maleki, J. He, S. Bochani, V. Nosrati, M.-A. Shahbazi and B. Guo, *ACS Nano*, 2021, **15**, 18895–18930.
- 6 H. Wang, Z. Xu, M. Zhao, G. Liu and J. Wu, *Biomater. Sci.*, 2021, **9**, 1530–1546.
- 7 S. Bochani, A. Kalantari-Hesari, F. Haghi, V. Alinezhad, H. Bagheri, P. Makvandi, M.-A. Shahbazi, A. Salimi, I. Hirata and V. Mattoli, *ACS Appl. Bio Mater.*, 2022, **5**, 4435–4453.
- 8 R. Kushwaha, S. Sharma, S. Kumar and A. Kumar, *Mater. Chem. Horiz.*, 2023, **2**, 11–39.
- 9 Y. Li, R. Fu, Z. Duan, C. Zhu and D. Fan, *ACS Nano*, 2022, **16**, 7486–7502.
- 10 W. Peng, D. Li, K. Dai, Y. Wang, P. Song, H. Li, P. Tang, Z. Zhang, Z. Li and Y. Zhou, *Int. J. Biol. Macromol.*, 2022, **208**, 400–408.
- 11 Y.-W. Ding, Z.-Y. Wang, Z.-W. Ren, X.-W. Zhang and D.-X. Wei, *Biomater. Sci.*, 2022, **10**, 3393–3409.
- 12 M. Abazari, T. Akbari, M. Hasani, E. Sharifikolouie, M. Raoufi, A. Foroumadi, M. Sharifzadeh, L. Firoozpour and M. Khoobi, *Carbohydr. Polym.*, 2022, 119808.
- 13 H. Hu and F.-J. Xu, *Biomater. Sci.*, 2020, **8**, 2084–2101.
- 14 P. Jaipan, A. Nguyen and R. J. Narayan, *MRS Commun.*, 2017, **7**, 416–426.
- 15 T. C. Tseng, L. Tao, F. Y. Hsieh, Y. Wei, I. M. Chiu and S. h. Hsu, *Adv. Mater.*, 2015, **27**, 3518–3524.
- 16 X.-H. Wang, F. Song, D. Qian, Y.-D. He, W.-C. Nie, X.-L. Wang and Y.-Z. Wang, *Chem. Eng. J.*, 2018, **349**, 588–594.
- 17 B. Tao, C. Lin, Y. Deng, Z. Yuan, X. Shen, M. Chen, Y. He, Z. Peng, Y. Hu and K. Cai, *J. Mater. Chem. B*, 2019, **7**, 2534–2548.
- 18 F. Wahid, Y.-N. Zhou, H.-S. Wang, T. Wan, C. Zhong and L.-Q. Chu, *Int. J. Biol. Macromol.*, 2018, **114**, 1233–1239.
- 19 H. Chen, C. Peng, L. Wang, X. Li, M. Yang, H. Liu, H. Qin and W. Chen, *Chem. Eng. J.*, 2021, **403**, 126341.
- 20 M. Li, X. Liu, L. Tan, Z. Cui, X. Yang, Z. Li, Y. Zheng, K. W. K. Yeung, P. K. Chu and S. Wu, *Biomater. Sci.*, 2018, **6**, 2110–2121.
- 21 P. Makvandi, M. Shabani, N. Rabiee, Q. K. Anjani, A. Maleki, E. N. Zare, A. H. B. Sabri, D. De Pasquale, M. Koskinopoulou and E. Sharifi, *Adv. Mater.*, 2023, 2210034.
- 22 T. Su, M. Zhang, Q. Zeng, W. Pan, Y. Huang, Y. Qian, W. Dong, X. Qi and J. Shen, *Bioact. Mater.*, 2021, **6**, 579–588.
- 23 D. Gan, T. Xu, W. Xing, X. Ge, L. Fang, K. Wang, F. Ren and X. Lu, *Adv. Funct. Mater.*, 2019, **29**, 1805964.
- 24 G. Gao, Y.-W. Jiang, H.-R. Jia and F.-G. Wu, *Biomaterials*, 2019, **188**, 83–95.
- 25 S. Barrientos, O. Stojadinovic, M. S. Golinko, H. Brem and M. Tomic-Canic, *Wound Repair Regen.*, 2008, **16**, 585–601.
- 26 T. N. Demidova-Rice, M. R. Hamblin and I. M. Herman, *Adv. Skin Wound Care*, 2012, **25**, 304.
- 27 S. Wei, P. Xu, Z. Yao, X. Cui, X. Lei, L. Li, Y. Dong, W. Zhu, R. Guo and B. Cheng, *Acta Biomater.*, 2021, **124**, 205–218.
- 28 T. Li, H. Lu, L. Zhou, M. Jia, L. Zhang, H. Wu and L. Shan, *Cell Proliferation*, 2022, **55**, e13212.
- 29 S. M. Oliveira, V. E. Santo, M. E. Gomes, R. L. Reis and J. F. Mano, *Biomaterials*, 2015, **48**, 56–65.
- 30 Z. Zheng, M. Li, P. Shi, Y. Gao, J. Ma, Y. Li, L. Huang, Z. Yang and L. Yang, *Bioact. Mater.*, 2021, **6**, 2613–2628.
- 31 J. Milstone, *Fed. Proc.*, 1964, **23**, 742–748.
- 32 N. Nayyar, H. Mannasian, L. Yang and H. Liu, *Essentials of Blood Product Management in Anesthesia Practice*, 2021, pp. 29–35.
- 33 E. Anitua, P. Nurden, R. Prado, A. T. Nurden and S. Padilla, *Biomaterials*, 2019, **192**, 440–460.

- 34 Y. Liu, K. Ai, J. Liu, M. Deng, Y. He and L. Lu, *Adv. Mater.*, 2013, **25**, 1353–1359.
- 35 L. Wang, X. Zhang, K. Yang, Y. V. Fu, T. Xu, S. Li, D. Zhang, L. N. Wang and C. S. Lee, *Adv. Funct. Mater.*, 2020, **30**, 1904156.
- 36 J. Qu, X. Zhao, P. X. Ma and B. Guo, *Acta Biomater.*, 2017, **58**, 168–180.
- 37 P. Yang, S. Zhang, N. Zhang, Y. Wang, J. Zhong, X. Sun, Y. Qi, X. Chen, Z. Li and Y. Li, *ACS Appl. Mater. Interfaces*, 2019, **11**, 42671–42679.
- 38 K. Musaie, S. Abbaszadeh, V. Nosrati-Siahmazgi, M. Qahremani, S. Wang, M. R. Eskandari, S. V. Niknezhad, F. Haghi, Y. Li and B. Xiao, *Biomater. Sci.*, 2023, **11**, 2486–2503.
- 39 Y. Liang, X. Zhao, T. Hu, B. Chen, Z. Yin, P. X. Ma and B. Guo, *Small*, 2019, **15**, 1900046.
- 40 Y. Chen, Y. Gao, Y. Chen, L. Liu, A. Mo and Q. Peng, *J. Controlled Release*, 2020, **328**, 251–262.
- 41 M.-C. Wu, A. R. Deokar, J.-H. Liao, P.-Y. Shih and Y.-C. Ling, *ACS Nano*, 2013, **7**, 1281–1290.
- 42 W. Ge, S. Cao, F. Shen, Y. Wang, J. Ren and X. Wang, *Carbohydr. Polym.*, 2019, **224**, 115147.
- 43 A. Chinnathambi, S. Ali Alharbi, D. Joshi and H. Lenin, *Bioinorg. Chem. Appl.*, 2022, **2022**, DOI: [10.1155/2022/9493816](https://doi.org/10.1155/2022/9493816).
- 44 F. Shahidi and Y. Zhong, *J. Funct. Foods*, 2015, **18**, 757–781.
- 45 M.-A. Shahbazi, M. Hamidi, E. M. Mäkilä, H. Zhang, P. V. Almeida, M. Kaasalainen, J. J. Salonen, J. T. Hirvonen and H. A. Santos, *Biomaterials*, 2013, **34**, 7776–7789.
- 46 X. Zhao, B. Guo, H. Wu, Y. Liang and P. X. Ma, *Nat. Commun.*, 2018, **9**, 2784.
- 47 Q. Huang, T. Wu, Y. Guo, L. Wang, X. Yu, B. Zhu, L. Fan, J. H. Xin and H. Yu, *Int. J. Biol. Macromol.*, 2023, **234**, 123722.
- 48 Y. Zhang, Z.-L. Wang, Z.-P. Deng, Z.-L. Wang, F. Song and L.-L. Zhu, *Carbohydr. Polym.*, 2023, 120973.
- 49 J. Zhou, Y. Liu, X. Liu, J. Wan, S. Zuo, T. Pan, Y. Liu, F. Sun, M. Gao and X. Yu, *Carbohydr. Polym.*, 2023, 120924.
- 50 N. Ninan, A. Forget, V. P. Shastri, N. H. Voelcker and A. Blencowe, *ACS Appl. Mater. Interfaces*, 2016, **8**, 28511–28521.
- 51 P. Atienza-Roca, D. C. Kieser, X. Cui, B. Bathish, Y. Ramaswamy, G. J. Hooper, A. N. Clarkson, J. Rnjak-Kovacina, P. J. Martens and L. M. Wise, *Biomater. Sci.*, 2020, **8**, 5005–5019.
- 52 T. Wang, W. Yi, Y. Zhang, H. Wu, H. Fan, J. Zhao and S. Wang, *Colloids Surf., B*, 2023, **222**, 113096.
- 53 Y. Zhang, Z.-L. Wang, Z.-P. Deng, Z.-L. Wang, F. Song and L.-L. Zhu, *Adv. Polym. Technol.*, 2022, **2022**, 1–11.
- 54 P. Zhang, Q. Xu, X. Li and Y. Wang, *Mater. Sci. Eng., C*, 2020, **108**, 110396.
- 55 X. Zhang, D. Yao, W. Zhao, R. Zhang, B. Yu, G. Ma, Y. Li, D. Hao and F. J. Xu, *Adv. Funct. Mater.*, 2021, **31**, 2009258.
- 56 S. Li, Q. Dong, X. Peng, Y. Chen, H. Yang, W. Xu, Y. Zhao, P. Xiao and Y. Zhou, *ACS Nano*, 2022, **16**, 11346–11359.
- 57 K. Lu, K. Li, M. Zhang, Z. Fang, P. Wu, L. Feng, K. Deng, C. Yu, Y. Deng and Y. Xiao, *Chem. Eng. J.*, 2021, **424**, 130429.
- 58 S. K. Papageorgiou, E. P. Kouvelos, E. P. Favvas, A. A. Sapalidis, G. E. Romanos and F. K. Katsaros, *Carbohydr. Res.*, 2010, **345**, 469–473.
- 59 S. Cao, X. Luo, X. Han, X. Lu and C. Zou, *Energies*, 2022, **15**, 824.
- 60 J. Amirian, T. T. T. Van, S.-H. Bae, H.-I. Jung, H.-J. Choi, H.-D. Cho and B.-T. Lee, *Int. J. Biol. Macromol.*, 2017, **105**, 143–153.
- 61 H. Omidian, J. G. Rocca and K. Park, *J. Controlled Release*, 2005, **102**, 3–12.
- 62 L. Yueqi, X. Jie, S. Ya, F. Huan, L. Jiaqi, L. Siyao, C. Y. Yee, N. Yi, L. Wenfang and P. Bo, *Int. J. Bioprint.*, 2023, **9**, DOI: [10.18063/ijb.v9i1.689](https://doi.org/10.18063/ijb.v9i1.689).
- 63 J. Li and D. J. Mooney, *Nat. Rev. Mater.*, 2016, **1**, 1–17.
- 64 Q. Tang, T. Lim, X.-J. Wei, Q.-Y. Wang, J.-C. Xu, L.-Y. Shen, Z.-Z. Zhu and C.-Q. Zhang, *Biomaterials*, 2020, **255**, 120138.
- 65 I. Garcia-Orue, E. Santos-Vizcaino, P. Sanchez, F. B. Gutierrez, J. J. Aguirre, R. M. Hernandez and M. Igartua, *Biomater. Adv.*, 2022, **135**, 112695.
- 66 C. Wang, C. Liang, R. Wang, X. Yao, P. Guo, W. Yuan, Y. Liu, Y. Song, Z. Li and X. Xie, *Biomater. Sci.*, 2020, **8**, 313–324.
- 67 Y. Liang, Z. Li, Y. Huang, R. Yu and B. Guo, *ACS Nano*, 2021, **15**, 7078–7093.
- 68 J. Chen, Y. Liu, G. Cheng, J. Guo, S. Du, J. Qiu, C. Wang, C. Li, X. Yang and T. Chen, *Small*, 2022, **18**, 2201300.
- 69 B. Tao, C. Lin, Z. Yuan, Y. He, M. Chen, K. Li, J. Hu, Y. Yang, Z. Xia and K. Cai, *Chem. Eng. J.*, 2021, **403**, 126182.
- 70 X. Zhu, W. Feng, J. Chang, Y.-W. Tan, J. Li, M. Chen, Y. Sun and F. Li, *Nat. Commun.*, 2016, **7**, 10437.
- 71 J. Huo, Q. Jia, H. Huang, J. Zhang, P. Li, X. Dong and W. Huang, *Chem. Soc. Rev.*, 2021, **50**, 8762–8789.
- 72 Q. Wei, Y. Wang, L. Jia, G. Ma, X. Shi, W. Zhang and Z. Hu, *Biomater. Sci.*, 2023, **11**, 170–180.
- 73 M. Schäfer and S. Werner, *Pharmacol. Res.*, 2008, **58**, 165–171.
- 74 Y. R. Girish, K. S. Sharathkumar, K. Prashantha, S. Rangappa and M. S. Sudhanva, *Mater. Chem. Horiz.*, 2023, DOI: [10.22128/MCH.2023.647.1037](https://doi.org/10.22128/MCH.2023.647.1037).
- 75 J. Hu, L. Yang, P. Yang, S. Jiang, X. Liu and Y. Li, *Biomater. Sci.*, 2020, **8**, 4940–4950.
- 76 F. Mollica, R. Lucernati and R. Amorati, *J. Mater. Chem. B*, 2021, **9**, 9980–9988.
- 77 L. He, G. Huang, H. Liu, C. Sang, X. Liu and T. Chen, *Sci. Adv.*, 2020, **6**, eaay9751.
- 78 V. Castrejón-Comas, C. Alemán and M. M. Pérez-Madrigal, *Biomater. Sci.*, 2023, **11**, 2266–2276.
- 79 J. I. Paez, A. de Miguel-Jiménez, R. Valbuena-Mendoza, A. Rathore, M. Jin, A. Glaser, S. Pearson and A. Del Campo, *Biomacromolecules*, 2021, **22**, 2874–2886.
- 80 M. Jin, G. Koçer and J. I. Paez, *ACS Appl. Mater. Interfaces*, 2022, **14**, 5017–5032.



- 81 K. S. Lim, Y. Ramaswamy, J. J. Roberts, M. H. Alves, L. A. Poole-Warren and P. J. Martens, *Macromol. Biosci.*, 2015, **15**, 1423–1432.
- 82 Y. Liang, J. He and B. Guo, *ACS Nano*, 2021, **15**, 12687–12722.
- 83 A. G. Goswami, S. Basu, F. Huda, J. Pant, A. Ghosh Kar, T. Banerjee and V. K. Shukla, *Growth Factors*, 2022, **40**, 73–88.
- 84 M. K. Lichtman, M. Otero-Vinas and V. Falanga, *Wound Repair Regen.*, 2016, **24**, 215–222.
- 85 Z. Qian, H. Wang, Y. Bai, Y. Wang, L. Tao, Y. Wei, Y. Fan, X. Guo and H. Liu, *ACS Appl. Mater. Interfaces*, 2020, **12**, 55659–55674.
- 86 C.-C. Liang, A. Y. Park and J.-L. Guan, *Nat. Protoc.*, 2007, **2**, 329–333.
- 87 E. Aiba-Kojima, N. H. Tsuno, K. Inoue, D. Matsumoto, T. Shigeura, T. Sato, H. Suga, H. Kato, T. Nagase and K. Gonda, *Wound Repair Regen.*, 2007, **15**, 511–520.
- 88 M. Simons, E. Gordon and L. Claesson-Welsh, *Nat. Rev. Mol. Cell Biol.*, 2016, **17**, 611–625.
- 89 Q. Zeng, Y. Qian, Y. Huang, F. Ding, X. Qi and J. Shen, *Bioact. Mater.*, 2021, **6**, 2647–2657.
- 90 J. Paez-Mayorga, S. Capuani, M. Farina, M. L. Lotito, J. A. Niles, H. F. Salazar, J. Rhudy, L. Esnaola, C. Y. X. Chua and F. Taraballi, *Adv. Healthcare Mater.*, 2020, **9**, 2000670.
- 91 Y. Liang, H. Xu, Z. Li, A. Zhangji and B. Guo, *Nano-Micro Lett.*, 2022, **14**, 185.
- 92 S. He, J. Fang, C. Zhong, F. Ren and M. Wang, *Acta Biomater.*, 2022, **140**, 149–162.